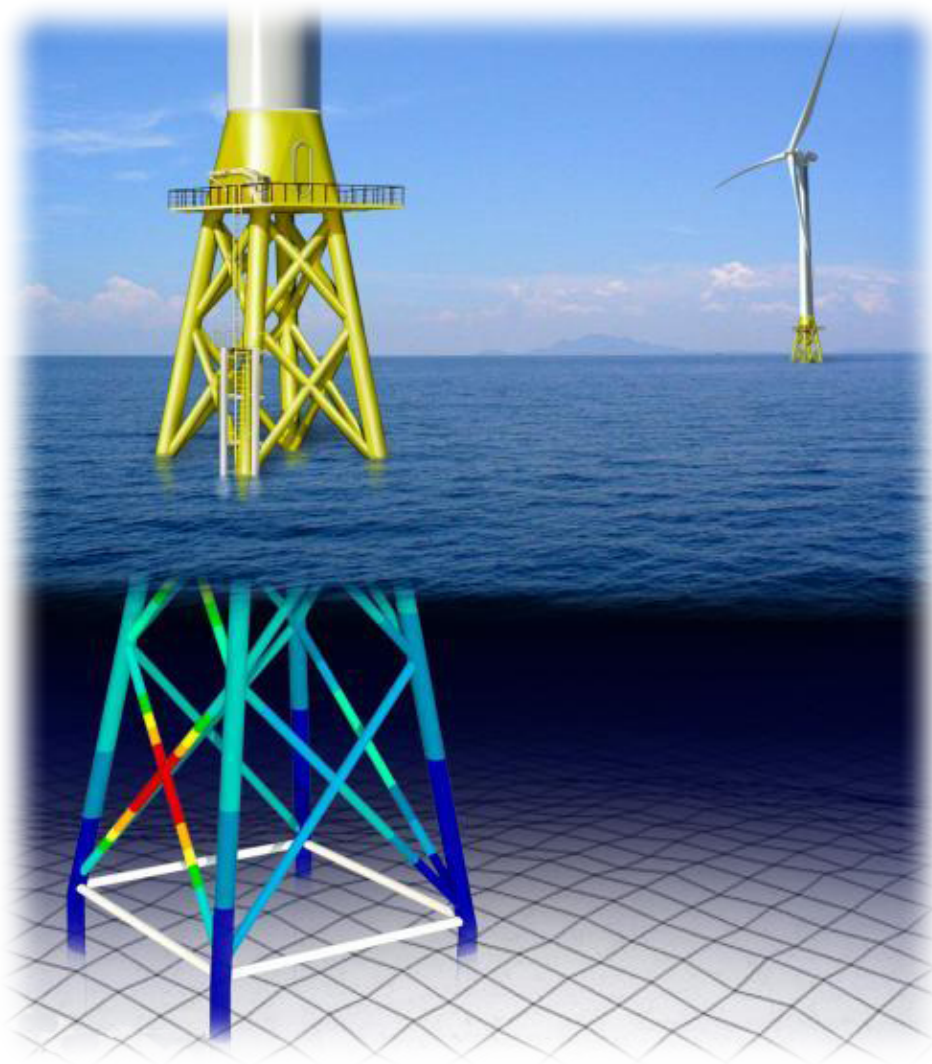


# Fatigue Analysis and Design Optimisation of Offshore Wind Turbine Support Structures

---



MASTER THESIS  
JONAS MATHIAS LAUSTSEN  
DESIGN OF MECHANICAL SYSTEMS  
AALBORG UNIVERSITY  
3 JUNE 2014



**School of-  
Engineering and Science  
Mechanical & Manufacturing  
Engineering**

Fibigerstraede 16  
9220 Aalborg East

Synopsis:

Title:

**Fatigue Analysis and Design  
Optimisation of Offshore Wind  
Turbine Support Structures**

Theme:

Master Thesis

Project period:

DMS4, spring semester 2014  
3 February - 3 June

Project group:

2.217b - Fib16

Participant:

---

Jonas Mathias Laustsen

Supervisor:

Erik Lund

Pages: 60 (49)

Appendices: 4

The aim of this project is to perform gradient based optimisation, with fatigue as constraint, on an offshore wind turbine support structure, with the goal of minimising the mass.

A finite element model, which utilises 3D Bernoulli-Euler beam elements, has been developed. The finite element model is applied to perform the structural analysis and determine the damage caused by the applied nonproportional loading history.

In order to handle nonproportional loading, a modified Wang-Brown counting method is applied, together with the Findley critical plane fatigue model.

The optimisation is performed using an SLP algorithm, with adaptive move limits, where the goal is to minimise the total mass of the structure subjected to a damage criterion, which is the Palmgren-Miner sum.

A design sensitivity analysis is performed in order to determine the gradient of the constraint function, which is done using a numerical and an analytical method. The analytical design sensitivity analysis is performed using the direct differentiation method, which is verified by a numerical central difference method.





# Preface

---

This project report is written by Jonas Laustsen during 4<sup>th</sup> semester of the master program in "Design of Mechanical Systems" at Aalborg University. The project concerns "Fatigue Analysis and Design Optimisation of Offshore Wind Turbine Support Structures".

In this project, the Harvard reference method is used, where sources are referenced by surname and year. Figures, tables, and equations are numbered according to the chapter number and with ascending numbers throughout the chapter, e.g. the first table in chapter two is denoted 2.1. Equation numbers are written within parenthesis. Symbols which are vectors and matrices are written within curly and square brackets, respectively. A global and local coordinate system is used, which is denoted  $x, y, z$  and  $x', y', z'$ , respectively.

A list of bibliography is found at page 59. The used nomenclature is found on page XI. The front page image is by Offshorewind.biz [2012].

The appendix and the appendix CD are included at the end of this document. The appendix CD contains the report as a PDF file, MATLAB-scripts, and ANSYS-scripts, as described in appendix D.



Dette projekt omhandler designoptimering af en støttestruktur til en vindmølle, hvor der tages hensyn til et udmattelseskriterie.

Der er udviklet en finite element bjælke model, som benyttes til den strukturelle analyse af støttestrukturen. I finite element modellen anvendes der 3D bjælke elementer som er baseret på Bernoulli-Euler bjælke teori. Spændingerne evalueres i udvalgte punkter i tværsnittet. Dette gøres for begge knuder i alle elementerne. Tværsnittet er modelleret som et tyndvægget cirkulært tværsnit. Finite element modellen er verificeret i henhold til en ANSYS model, hvor de globale flytninger, spændingerne i tværsnittet og egenfrekvenserne er blevet sammenlignet. Der viste sig at være god overensstemmelse mellem de to modeller. Dog følger ANSYS' måde at regne tværspændingerne i tværsnittet ikke bjælketeorien.

Støttestrukturen er pålagt en lastserie, som er simuleret for en generisk 5MW vindmølle. Lasterne er ikke proportionelle, hvormed der skal anvendes en speciel tællemetode for at tage hensyn til effekten af de ikke proportionelle laster. Her anvendes en modificerede Wang-Brown rainflow tællemetode, hvilket er implementeret finite element koden. Tællemetoden anvendes til at bestemme hvor mange gange et givet lastinterval optræder, ud fra den pålagte lastserie. Der regnes en samlet skade i hvert evaluerings punkt i tværsnittet, dette gøres vha. Palmgren-Miners lineære delskade.

Der anvendes en critical plane udmattelse model til bestemmelse af hvor mange belastninger der skal til, før der opstår brud ved et given spændingsniveau. Denne critical plane model kan bestemme hvornår materialet bryder og i hvilken vinkel brudplanet ligger. Her anvendes Findley udmattelses modellen, den har til fordel at, antallet af belastninger før brud kan isoleres i udtrykket, hvilket muliggør at skade sensitiviteten kan regnes analytisk.

Der er anvendt en gradient baseret optimerings metode, hvor objektfunktionen er en funktion af den samlede masse for strukturen. Som bibetingelse skal det overholdes at skaden ikke må overskride et givent niveau i et af evalueringenspunkter. Bibetingelserne er opstillet som en skade der er beregnet vha. Palmgren-Miners delskade. Som input til den gradient baseret optimering, kræves at gradienten af objektfunktionen og gradienten af bibetingelserne er bestemt. Disse bestemmes vha. en følsomheds analyse, hvor gradienterne er regnet analytisk ved brug af en direkte differentiations metode. De implementerede gradienter verificeres ved sammenligning med gradienter bestemt vha. en approksimativ metode. Pga. en meget ulineær betingelses funktion, har det været nødvendigt at anvende en SLP algoritme, der går ind og lineariseret problemet i et lille interval, hvormed løsningen i dette interval dernæst bliver det nye startgæt. For at afprøve implementeringen er optimeringen massen af en fast indspændt bjælke, som er pålagt en ikke proportionel lastserie, blevet minimeret.



# Contents

---

|                    |   |               |
|--------------------|---|---------------|
| <b>Chapter 1</b>   | <b>Introduction</b>                                   | <b>1</b>      |
| 1.1                | Problem statement . . . . .                           | 3             |
| <br><b>Part I</b>  |   | <br><b>5</b>  |
| <b>Chapter 2</b>   | <b>FE Model</b>                                       | <b>7</b>      |
| 2.1                | 3D beam element . . . . .                             | 7             |
| 2.1.1              | Element stiffness matrix . . . . .                    | 8             |
| 2.1.2              | Transformation matrix . . . . .                       | 9             |
| 2.2                | Assembly of global stiffness matrix . . . . .         | 10            |
| 2.3                | Element loads . . . . .                               | 11            |
| 2.4                | Calculation of cross-sectional stresses . . . . .     | 12            |
| 2.5                | Jacket model . . . . .                                | 14            |
| 2.5.1              | Loading history . . . . .                             | 15            |
| <b>Chapter 3</b>   | <b>Verification of FEM code</b>                       | <b>19</b>     |
| 3.1                | Natural frequency . . . . .                           | 19            |
| 3.2                | Global displacement . . . . .                         | 21            |
| 3.3                | Stress . . . . .                                      | 22            |
| 3.3.1              | Normal stress . . . . .                               | 22            |
| 3.3.2              | Shear stress . . . . .                                | 23            |
| <b>Chapter 4</b>   | <b>Fatigue</b>  | <b>25</b>     |
| 4.1                | Proportional and Nonproportional loading . . . . .    | 25            |
| 4.2                | Counting method for nonproportional loading . . . . . | 26            |
| 4.2.1              | Mean and alternating components . . . . .             | 30            |
| 4.3                | Multiaxial fatigue . . . . .                          | 31            |
| 4.4                | Palmgren-Miner linear damage rule . . . . .           | 33            |
| <br><b>Part II</b> |   | <br><b>35</b> |
| <b>Chapter 5</b>   | <b>Introduction</b>                                   | <b>37</b>     |
| 5.1                | Design variables . . . . .                            | 37            |
| 5.2                | Cost function and constraints . . . . .               | 38            |
| <b>Chapter 6</b>   | <b>Design Sensitivity Analysis</b>                    | <b>41</b>     |
| 6.1                | Finite difference method . . . . .                    | 41            |
| 6.2                | Direct differentiation method . . . . .               | 42            |
| <b>Chapter 7</b>   | <b>Verification of design sensitivity analysis</b>    | <b>45</b>     |
| 7.1                | Cost sensitivity . . . . .                            | 46            |
| 7.2                | Displacement sensitivity . . . . .                    | 47            |

|  |               |
|--|---------------|
| 7.3 Stress sensitivity . . . . .                                       | 47            |
| 7.4 Constraint sensitivity . . . . .                                   | 48            |
| <b>Chapter 8 Implementation and results</b>                            | <b>51</b>     |
| <br><b>Part III Evaluation</b>   | <br><b>53</b> |
| <b>Chapter 9 Conclusion</b>  | <b>55</b>     |
| <b>Chapter 10 Discussion</b>   | <b>57</b>     |
| <b>Bibliography</b>  | <b>59</b>     |
| <br><b>Part IV Appendix</b>  | <br><b>1</b>  |
| <b>Appendix A ANSYS model</b>  | <b>3</b>      |
| <b>Appendix B DSA derivations</b>                                      | <b>5</b>      |
| <b>Appendix C Plot for verification of design sensitivity analysis</b> | <b>17</b>     |
| <b>Appendix D Appendix CD</b>  | <b>23</b>     |

# Nomenclature

| Symbol:      | Description:  | Unit:             |
|--------------|---|-------------------|
| $A_e$        | Cross-sectional area of element                     | [m <sup>2</sup> ] |
| $E$          | Young's modulus                                     | [Pa]              |
| $G$          | Shear modulus                                       | [Pa]              |
| $I_y$        | Area moment of inertia w.r.t. the y-axis            | [m <sup>4</sup> ] |
| $I_z$        | Area moment of inertia w.r.t. the z-axis            | [m <sup>4</sup> ] |
| $J_x$        | Polar moment of inertia w.r.t. the x-axis           | [m <sup>4</sup> ] |
| $L_e$        | Length of the element                               | [m]               |
| $M_y$        | Moment about y' axis                                | [Nm]              |
| $M_z$        | Moment about z' axis                                | [Nm]              |
| $N_e$        | Number of elements                                  | [-]               |
| $N_x$        | Normal force along x' axis                          | [N]               |
| $Q_y$        | First moment in the y-direction                     | [m <sup>3</sup> ] |
| $Q_z$        | First moment in the z-direction                     | [m <sup>3</sup> ] |
| $R_m$        | Mean radius   | [m]               |
| $R$          | Radius  | [m]               |
| $T_x$        | Torque about the x' axis                            | [Nm]              |
| $V_y$        | Shear force in the y' direction                     | [N]               |
| $V_z$        | Shear force in the z' direction                     | [N]               |
| $[I]$        | Identity matrix                                     | [-]               |
| $[K]$        | Global stiffness matrix                             | [-]               |
| $[M]$        | Global mass matrix                                  | [-]               |
| $[T]$        | Transformation matrix                               | [-]               |
| $[\Lambda]$  | Rotation matrix                                     | [-]               |
| $[{}_gK_e]$  | Element stiffness matrix transformed                | [-]               |
| $[{}_lK_e]$  | Local element stiffness matrix                      | [-]               |
| $\Delta x_i$ | Perturbation of the i <sup>th</sup> design variable | [-]               |
| $\beta$      | Angle of sample point in the cross-section          | [deg]             |
| $\gamma$     | Shear strain  | [-]               |

*Continued on next page*

| Symbol:      | Description:  | Unit:                                       |
|--------------|---|---|
| $\kappa_y$   | Curvature about y-axis  | [1/m]                                       |
| $\kappa_z$   | Curvature about z-axis  | [1/m]                                       |
| $f$          | General response function   | [-]   |
| $\nu$        | Poisson's ratio   | [-]   |
| $\omega_i$   | Natural frequency   | [rad/s]                                     |
| $\bar{\nu}$  | Effective poisson's ratio,  | [-]   |
| $\rho$       | Density   | $\left[\frac{\text{kg}}{\text{m}^3}\right]$ |
| $\sigma$     | Normal stress   | [Pa]  |
| $\tau'_f$    | Torsional fatigue strength  | [-]   |
| $\tau_f^*$   | Corrected torsional fatigue strength  | [-]   |
| $\tau$       | Shear stress  | [Pa]  |
| $d$          | Outer diameter  | [m]   |
| $f(\{x\})$   | Cost function as a function of design variables                                     | [-]   |
| $f$          | Fatigue constant for given material   | [Pa]  |
| $g^0$        | Ideal value   | [-]   |
| $g_j(\{x\})$ | Constraint function as a function of design variables                               | []  |
| $k$          | Material constant which is related to the materials' sensitivity to normal stresses | [-]   |
| $m$          | Mass  | [kg]  |
| $p$          | Coefficient to scale most violated constraint                                       | [-]   |
| $t$          | Wall thickness  | [m]   |
| $w_j$        | Weight factor   | [-]   |
| $\{D_e\}$    | Local element displacement vector   | [-]   |
| $\{D\}$      | Global displacement vector  | [-]   |
| $\{R\}$      | Global load vector  | [-]   |
| $\{X\}$      | Eigenvector   | [-]   |
| $\{c\}$      | Gradient of cost function w.r.t. design variables                                   | [-]   |
| $\{x\}$      | Design variable vector  | [-]   |



# Introduction

# 1

This project examines the subject of how to perform a design optimisation, with fatigue as constraint, of an offshore wind turbine support structure.

The offshore wind turbine is mounted on a support structure which is connected to a foundation on the seabed. The foundation ensures that the wind turbine is securely fixed at the seabed. There are mainly two ways of supporting offshore wind turbines, the first is to construct a floating support structure which is by wires anchored at the bottom of the seabed. The second way is to construct a support structure which is in contact with the seabed, either secured by a foundation or by gravity. The support structures are typically welded steel structures. [LORC, 2011]

A popular support structure for shallow waters, 20-30 m, is the monopile support structure. It is used because of its simple construction, where the tube has a diameter of 2-5 m with a wall thickness of up to 100 mm. The limitation of this support structure type is the structural strength compared to the production cost at greater water depths. To maintain the structural requirements, such as bending stiffness, natural frequency, and mass at larger water depths, the design of monopile structure will require the cross-sectional parameters to increase. The increased cross-section and water depth increase the mass of the support structure, which increases the cost of the support structure.

The tripod support structure is a modified version of the monopile support structure. The loads at the foundation are distributed by three jackets, which increase the strength, where the bending moment is highest, of the support structure.

The jacket structure is a commonly used offshore support structure in the oil and gas industry, e.g. oil platforms. It is also used for supporting the offshore wind turbine at water depths of up to 50 m. It is a frame structure with three or four legs, where trusses between the legs form a grid, which stiffens the construction. This type of support structure is assembled onshore and shipped out for installation. The frame structure is larger than the one of the monopile tubes, but the dimension of each truss is much smaller, which makes it easier to handle during the production.

For deep waters, a floating support structure can be used. However, the construction for supporting the wind turbine has to be large, in order to stabilise the dynamic loads from the waves and wind hitting the blades and carry the static load from the tower, nacelle, and blades.

The four support structure concepts described above are shown in figure 1.1. The first three (from left to right) support structure concepts are in contact with the seabed, whereas the fourth concept is a floating support structure which is secured by wires connected to the seabed.

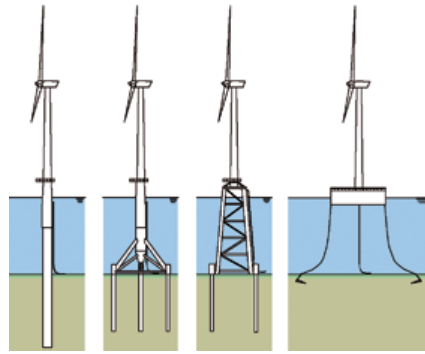


**Figure 1.1** Support structure concepts. From left to right: monopile, tripod, jacket, and floating structure. [UpWind, 2011]

The cost of the support structure for a offshore wind turbine is approximately 20% of the total cost [Lund and Overgaard, 2014]. This makes it crucial for the wind turbine manufacturers to minimise the cost of one support structure in order to gain a better and more competitive product. Since, a lot of material is used in making a support structure, the cost can be reduced by minimising the mass of the support structure. Because of the harsh offshore environment, it makes great demands to the support structure, that being time dependent wind and wave loads. The wave loads would affect the whole support structure and the wave loads would mostly affect the wind turbine which would transmit the transient loads to the support structure. The loads are applied in the 3D space and the components will not be in-phase, which introduces the concept of nonproportional loading. The nonproportional loading, from a fatigue point-of-view, has an influence in the fatigue life of the structure, therefore a proper fatigue model has to be used. Another thing which has a significant impact in the fatigue life, is corrosion. Since the support structure is submerged in salt water and made in steel, corrosion can not be ignored. Although, a high safety factor might be used to account for this, it is better to know the system and include the right theory in order to obtain a useful model.

In this project a jacket type support structure is considered, where the geometry from the UpWind project is used. The UpWind jacket support structure is designed to be used with the NREL 5-MW baseline wind turbine in 50 m of water. The NREL 5-MW baseline wind turbine has been developed as a standardised wind turbine model for easier comparison, which is described in Jonkman et al. [2009]. The UpWind jacket support structure has four legs, where the legs are connected by X-braces. The four legs are connected to four foundation piles, which are 45 m into the seabed. The UpWind jacket structure is illustrated in figure 1.2. At the top of the jacket structure a transition piece made of concrete is connecting the jacket structure with the wind turbine tower, as shown in figure 1.3.[Vorpahl et al., 2011]

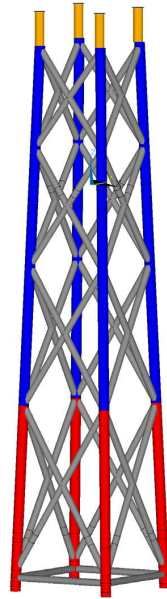


**Figure 1.2** Sketch of the UpWind jacket support structure, where the yellow pipes are embedded in the concrete, as shown in figure 1.3. [Vorpahl et al., 2011]

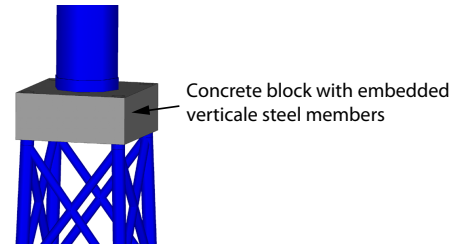


**Figure 1.3** Concrete transition piece which is connecting the jacket support structure with the wind turbine tower. [Vorpahl et al., 2011, Modified]

## 1.1 Problem statement

As stated in the introduction, the mass of the support structure has the potential to be reduced considerably, with the benefit of using less material and therefore reducing the cost. The aim of this project is to:

*Perform gradient based optimisation, with fatigue as constraint, on an offshore wind turbine support structure, with the goal of minimising the mass.*

The framework by Jørgensen and Nissen [2013] is used as a reference for comparison, however a new model is developed during this project period. The geometry from the UpWind jacket support structure will be used, however the cross-sectional parameters are not preserved. A linear FE model of the jacket structure is conducted and wind-based loads from a 600 s simulation with HAWC2[Energy, N/A] is applied. Wave loads acting on the support structure are not considered, even though they influence the fatigue life of the structure. A multiaxial rainflow counting method, which is able to handle nonproportional loading conditions [Meggiolaro and de Castro, 2011b] is used to count the stresses. The Findley fatigue model is used to access the fatigue life of the multiaxial and nonproportional loads. The mass of the jacket support structure is minimised by use of gradient based optimisation, where the gradients of the cost and constraints are calculated analytically using the direct differentiation method and evaluated in comparison with the overall finite difference method.



Part I

# Structural Analysis



# FE Model 2

The jacket structure is a frame like structure, which is modelled with 3D beam elements. It is assessed that the deformations of the jacket structure are small, by which the structural analysis is performed by a linear finite element analysis (FEM). The FEM is coded in MATLAB and verified by an equivalent analysis performed in ANSYS, as described in chapter 3.

The linear system of equations that has to be solved, in order to achieve the displacements, are defined in equation (2.1). The assembly of the global stiffness matrix is described in section 2.2.

$$[K] \{D\} = \{R\} \quad (2.1)$$

where:

|         |                                 |
|---------|---------------------------------|
| $[K]$   | Global stiffness matrix, [-]    |
| $\{D\}$ | Global displacement vector, [-] |
| $\{R\}$ | Global load vector, [-]         |

One of the advantages of using a linear model is that the principle of superposition is valid, by which the displacements from multiple load configurations can be added together in order to determine the resulting displacements. Another advantage is that the displacements are scalable according to the loads, since the displacements and the applied loads are proportional as seen in equation (2.1). By which the displacements of the model can be solved for six unity loading configurations, e.g. one loading configuration is a unity force in the x-direction and another is a unity moment about the x-axis. Afterwards, the displacements, from the unity loads, are scaled according to the applied load. This way, the FE model only have to be solved for six times, which results in low calculation times.

The unity scaling can be applied throughout the whole model, since the stresses are calculated from the displacements and the fatigue life is calculated from the stresses. By which the calculation of the sensitivities w.r.t. displacements, stresses, and fatigue life can be calculated efficiently. The calculation of sensitivities are described in chapter 6.

## 2.1 3D beam element

The 3D beam element is a two node element with six degrees of freedom in each node, as seen in figure 2.1.

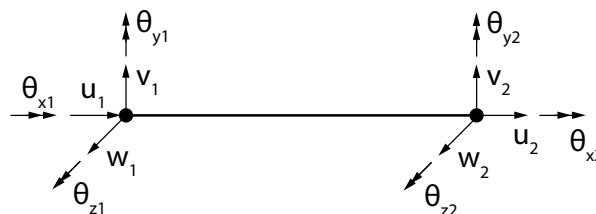


Figure 2.1 3D beam element dof.

The twelve degrees of freedom for the element are arranged in the displacement vector as follows:

$$\{D_e\} = \{u_1 \quad v_1 \quad w_1 \quad \theta_{x1} \quad \theta_{y1} \quad \theta_{z1} \quad u_2 \quad v_2 \quad w_2 \quad \theta_{x2} \quad \theta_{y2} \quad \theta_{z2}\}^T \quad (2.2)$$

### 2.1.1 Element stiffness matrix

The stiffness matrix of the 3D beam element is presented in equation (2.3). The element is based on the Bernoulli-Euler beam theory, which assumes; small displacements and rotations, the cross-section remain straight before and after deformation, the transverse normals are inextensible, and that the transverse normals remain perpendicular to the neutral line.

The element stiffness matrix for the 3D beam element is derived based on the following shape function interpolations. The lengthwise displacement and rotation are interpolated with a linear variation, whereas the displacements in y' and z' and rotation about y' and z' are interpolated with a cubic variation. This is due to the tangential requirement of the displacement field that has to be continuous, whereas the lengthwise displacement and rotation fields only have to be continuous.

$$[{}_lK_e] = \begin{bmatrix} X & 0 & 0 & 0 & 0 & 0 & -X & 0 & 0 & 0 & 0 & 0 \\ & Y_1 & 0 & 0 & 0 & Y_2 & 0 & -Y_1 & 0 & 0 & 0 & Y_2 \\ & & Z_1 & 0 & -Z_2 & 0 & 0 & 0 & -Z_1 & 0 & -Z_2 & 0 \\ & & & S & 0 & 0 & 0 & 0 & 0 & -S & 0 & 0 \\ & & & & Z_3 & 0 & 0 & 0 & Z_2 & 0 & Z_4 & 0 \\ & & & & & Y_3 & 0 & -Y_2 & 0 & 0 & 0 & Y_4 \\ & & & & & & X & 0 & 0 & 0 & 0 & 0 \\ & & & & & & & Y_1 & 0 & 0 & 0 & -Y_2 \\ & & \text{Sym.} & & & & & & Z_1 & 0 & Z_2 & 0 \\ & & & & & & & & & S & 0 & 0 \\ & & & & & & & & & & Z_3 & 0 \\ & & & & & & & & & & & Y_3 \end{bmatrix} \quad (2.3)$$

where  $[{}_lK_e]$  is the element stiffness matrix and  $X$ ,  $S$ ,  $Y_i$ , and  $Z_i$  are defined as:

$$\begin{aligned} X &= \frac{A_e E}{L_e} & S &= \frac{G J_x}{L_e} \\ Y_1 &= \frac{12 E I_z}{L_e^3} & Z_1 &= \frac{12 E I_y}{L_e^3} \\ Y_2 &= \frac{6 E I_z}{L_e^3} & Z_2 &= \frac{6 E I_y}{L_e^3} \\ Y_3 &= \frac{4 E I_z}{L_e} & Z_3 &= \frac{4 E I_y}{L_e} \\ Y_4 &= \frac{2 E I_z}{L_e} & Z_4 &= \frac{2 E I_y}{L_e} \end{aligned} \quad (2.4)$$



where:

[Cook et al., 2001, p. 27,  $\phi = 0$ ]

|       |   |
|-------|---|
| $A_e$ | Cross-sectional area of element, $[\text{m}^2]$           |
| $L_e$ | Length of the element, $[\text{m}]$                       |
| $E$   | Young's modulus, $[\text{Pa}]$                            |
| $G$   | Shear modulus, $[\text{Pa}]$                              |
| $I_y$ | Area moment of inertia w.r.t. the y-axis, $[\text{m}^4]$  |
| $I_z$ | Area moment of inertia w.r.t. the z-axis, $[\text{m}^4]$  |
| $J_x$ | Polar moment of inertia w.r.t. the x-axis, $[\text{m}^4]$ |

### 2.1.2 Transformation matrix

In figure 2.2 the topology for the 3D beam element is presented. A third node is required to define the orientation of the element, if the element is arbitrary oriented in space. The three nodes define the beam plane, which in the figure is grey. It is assumed that global coordinates,  $x$   $y$   $z$ , of the three nodes are known beforehand as shown by the  $\{a\}$ ,  $\{b\}$ , and  $\{c\}$  vectors.

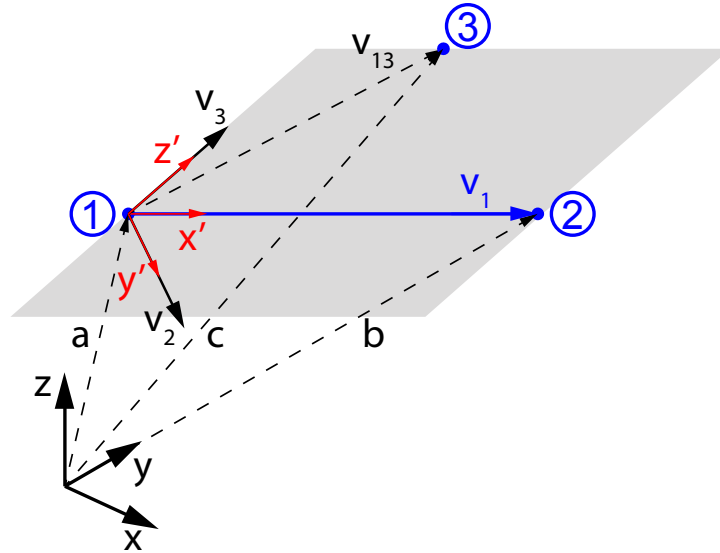


**Figure 2.2** Topology for the three node 3D beam element.

The method used for defining the local coordinate system,  $x'$   $y'$   $z'$ , of the beam element is inspired by Stærdahl [2008] and is adapted to match the transformation used in ANSYS for easier comparison. The local  $\{x'\}$ -axis is always collinear with the longitudinal axis of the beam element and the local origin is at node 1. The vectors  $\{v_1\}$  and  $\{v_{13}\}$  are defined as:

$$\{v_1\} = \{b\} - \{a\} \quad (2.5)$$

$$\{v_{13}\} = \{c\} - \{a\} \quad (2.6)$$

which is used to determine the two perpendicular vectors with respect to  $\{v_1\}$ :

$$\{v_2\} = \{v_{13}\} \times \{v_1\} \quad (2.7)$$

$$\{v_3\} = \{v_1\} \times \{v_2\} \quad (2.8)$$

The  $\{v_1\}$ ,  $\{v_2\}$ , and  $\{v_3\}$  vectors are collinear with the local  $\{x'\}$ ,  $\{y'\}$ , and  $\{z'\}$ , by which the unit vectors are found:

$$\begin{aligned}\{x'\} &= \frac{\{v_1\}}{|\{v_1\}|} \\ \{y'\} &= \frac{\{v_2\}}{|\{v_2\}|} \\ \{z'\} &= \frac{\{v_3\}}{|\{v_3\}|}\end{aligned}\tag{2.9}$$

The rotation from the global coordinate system to the local coordinate system is defined by the following rotation matrix:

$$[\Lambda] = \begin{bmatrix} \{x'\}^T \\ \{y'\}^T \\ \{z'\}^T \end{bmatrix}\tag{2.10}$$

By applying the rotation matrix to displacements and rotation for both end nodes of the beam element, the following transformation matrix is defined:

$$[T] = \begin{bmatrix} [\Lambda] & 0 & 0 & 0 \\ 0 & [\Lambda] & 0 & 0 \\ 0 & 0 & [\Lambda] & 0 \\ 0 & 0 & 0 & [\Lambda] \end{bmatrix}\tag{2.11}$$

The transformation matrix is applied to the local stiffness matrix, such that the local stiffness matrix is transformed in accordance with the global coordinate system.

$$[_gK_e] = [T]^T [_lK_e] [T]\tag{2.12}$$

## 2.2 Assembly of global stiffness matrix

The assembly of the global stiffness matrix,  $[K]$ , is conducted by a summation of all the element stiffness matrices,  $[_gK_e]$ :

$$[K] = \sum_{i=1}^{N_e} [_gK_e]_i\tag{2.13}$$

where:

$$N_e \mid \text{Number of elements, [-]}$$

The summation of the element stiffness matrices are performed by adding the nodal related stiffness components from the element stiffness matrix into the global stiffness matrix.

In order to illustrate the assembly of the global stiffness matrix, the following example is given. A simple 2D model with three truss elements where each element has two nodes is considered. The simple 2D model is seen in figure 2.3. The truss element has four DOF's, translation in x and y-direction in each node, by which the element stiffness matrix is a 4 by 4 matrix. The global stiffness matrix is constructed from the three element stiffness matrices, which results in a 6 by 6 matrix.

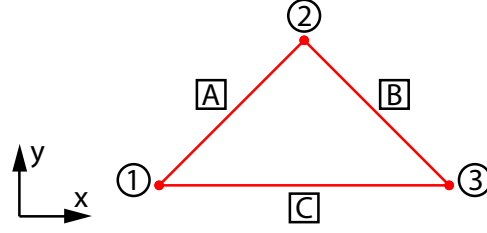


**Figure 2.3** Simple 2D truss model with three elements. The node numbers are circled and the element letters are squared.

The element stiffness matrices for the three truss elements are shown in equation (2.14). The components in the matrices are named, in lower case, according to the figure above. The actual values of the element stiffness matrices are not important in the process of describing the assembly of the global stiffness matrix. However it is necessary to locate the nodal relation of the matrix components with the associated DOF, which is why the associated DOF is listed at the upper and left borders of the element stiffness matrices.

$$\begin{array}{c}
 \begin{array}{c} u_1 \\ v_1 \\ u_2 \\ v_2 \end{array} \begin{bmatrix} a_{11} & a_{12} & a_{13} & a_{14} \\ a_{21} & a_{22} & a_{23} & a_{24} \\ a_{31} & a_{32} & a_{33} & a_{34} \\ a_{41} & a_{42} & a_{43} & a_{44} \end{bmatrix} \quad
 \begin{array}{c} u_2 \\ v_2 \\ u_3 \\ v_3 \end{array} \begin{bmatrix} b_{11} & b_{12} & b_{13} & b_{14} \\ b_{21} & b_{22} & b_{23} & b_{24} \\ b_{31} & b_{32} & b_{33} & b_{34} \\ b_{41} & b_{42} & b_{43} & b_{44} \end{bmatrix} \quad
 \begin{array}{c} u_1 \\ v_1 \\ u_3 \\ v_3 \end{array} \begin{bmatrix} c_{11} & c_{12} & c_{13} & c_{14} \\ c_{21} & c_{22} & c_{23} & c_{24} \\ c_{31} & c_{32} & c_{33} & c_{34} \\ c_{41} & c_{42} & c_{43} & c_{44} \end{bmatrix}
 \end{array} \quad (2.14)$$

The global stiffness matrix of the 2D truss model is shown in equation (2.15). The three element stiffness matrices from equation (2.14) have been summed, by which the associated matrix components are added.

$$\begin{array}{c}
 \begin{array}{c} u_1 \\ v_1 \\ u_2 \\ v_2 \\ u_3 \\ v_3 \end{array} \begin{bmatrix} a_{11} + c_{11} & a_{12} + c_{12} & a_{13} & a_{14} & c_{13} & c_{14} \\ a_{21} + c_{21} & a_{22} + c_{22} & a_{23} & a_{24} & c_{23} & c_{24} \\ a_{31} & a_{32} & a_{33} + b_{11} & a_{34} + b_{12} & b_{13} & b_{14} \\ a_{41} & a_{42} & a_{33} + b_{21} & a_{34} + b_{22} & b_{23} & b_{24} \\ c_{31} & c_{32} & b_{31} & b_{32} & b_{33} + c_{33} & b_{34} + c_{34} \\ c_{41} & c_{42} & b_{41} & b_{42} & b_{43} + c_{43} & b_{44} + c_{44} \end{bmatrix}
 \end{array} \quad (2.15)$$

## 2.3 Element loads

The applied loads on the element and parameters used in the calculation of the cross-sectional stresses are presented in this section. All loads are in accordance with the local coordinate of

the element. The axial and shear forces and the torque about  $x'$  are given as:

$$N_x = A_e \frac{u_2 - u_1}{L_e} \quad (2.16)$$

$$V_z = E I_y \frac{d^3 w}{dx^3} \quad (2.17)$$

$$V_y = E I_y \frac{d^3 v}{dx^3} \quad (2.18)$$

$$T_x = G J_x \frac{\theta_{x2} - \theta_{x1}}{L_e} \quad (2.19)$$

where the derivatives of  $w(x)$  and  $v(x)$  are given as:

$$\frac{d^3 w}{dx^3} = \frac{-12}{L_e^2} w_1 + \frac{6}{L_e} \theta_{y1} + \frac{12}{L_e^2} w_2 + \frac{6}{L_e} \theta_{y2} \quad (2.20)$$

$$\frac{d^3 v}{dx^3} = \frac{12}{L_e^2} v_1 + \frac{6}{L_e} \theta_{z1} + \frac{-12}{L_e^2} v_2 + \frac{6}{L_e} \theta_{z2} \quad (2.21)$$

The moments about  $z'$  and  $y'$  are given as:

$$M_z = E I_z \kappa_y \quad (2.22)$$

$$M_y = E I_y \kappa_z \quad (2.23)$$

where the curvatures of  $w(x)$  and  $v(x)$  are given as:

$$\kappa_z = \frac{12x - 6}{L_e^2} v_1 + \frac{6x - 4}{L_e} \theta_{z1} + \frac{-12x + 6}{L_e^2} v_2 + \frac{6x - 2}{L_e} \theta_{z2} \quad (2.24)$$

$$\kappa_y = \frac{-12x + 6}{L_e^2} w_1 + \frac{6x - 4}{L_e} \theta_{y1} + \frac{12x - 6}{L_e^2} w_2 + \frac{6x - 2}{L_e} \theta_{y2} \quad (2.25)$$

## 2.4 Calculation of cross-sectional stresses

In this section the calculation of the cross-sectional stresses are described. The stresses are evaluated by use of beam theory. Since the FE model is linear, the principle of superposition can be applied and thereby the normal stress contribution from the axial load and bending loads can be summed. Likewise, torsional and shear force shear stresses can be summed. The cross-section shown in figure 2.4 illustrates where the stresses are calculated.

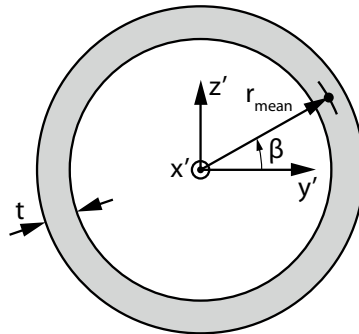


**Figure 2.4** Sketch of thin walled circular cross-section, where the angle  $\beta$  is used for the sample points around the cross-section.

The normal and shear stresses are evaluated by the following equations:

$$\sigma_N = \frac{N_x}{A_e} - \frac{M_z R_m \cos(\beta)}{I_z} + \frac{M_y R_m \sin(\beta)}{I_y} \quad (2.26)$$

$$\tau_{tot} = \tau_{xy} + \tau_{xz} \quad (2.27)$$

where the shear stress components are given as a sum of the contribution from the shear force and the torque:

$$\tau_{xy} = \frac{V_y Q_y}{I_z 2 b(\beta)} + \frac{T_x R_m \sin(\beta)}{J_x} \quad (2.28)$$

$$\tau_{xz} = \frac{V_z Q_z}{I_y 2 b(90^\circ - \beta)} + \frac{T_x R_m \cos(\beta)}{J_x} \quad (2.29)$$

The first moments  $Q_y$  and  $Q_z$  are the first moment of the cross-sectional above the point where the shear stress is evaluated. For the circular hollow tube, the first moments are given by:

$$Q_y = 2 \beta t \frac{R_m^2 \sin(\beta)}{\beta} \quad (2.30)$$

$$Q_z = 2 (90^\circ - \beta) t \frac{R_m^2 \sin(90^\circ - \beta)}{90^\circ - \beta} \quad (2.31)$$

[Gere and Goodno, 2009, p. 945]

The effective width of the cross-section is derived as a piece-wise function, where figure 2.5 shows the two parts. The expression for a circle is used, where the horizontal width of the inner circle is subtracted from the outer circle, by which the following is derived:

$$b(\beta) = \begin{cases} \sqrt{R^2 - (R_m \cos(\beta))^2} - \sqrt{r^2 - (R_m \cos(\beta))^2}, & R_m \cos(\beta) \leq r \\ \sqrt{R^2 - (R_m \cos(\beta))^2}, & r < R_m \cos(\beta) \leq R \end{cases} \quad (2.32)$$

The effective width is plotted as a function of  $\beta$  in figure 2.6.

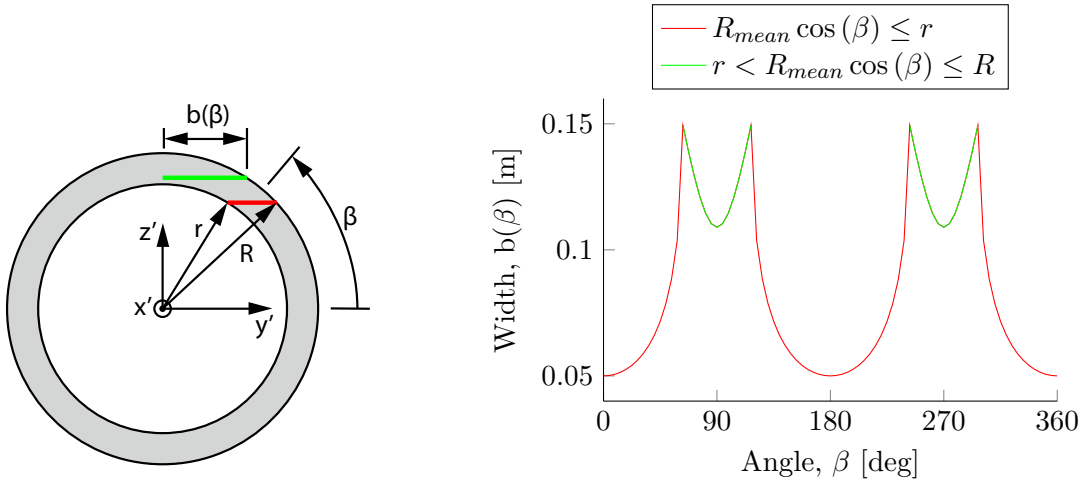


**Figure 2.5** Sketch of thin walled circular cross-section, which illustrates where width,  $b(\beta)$ , is measured.

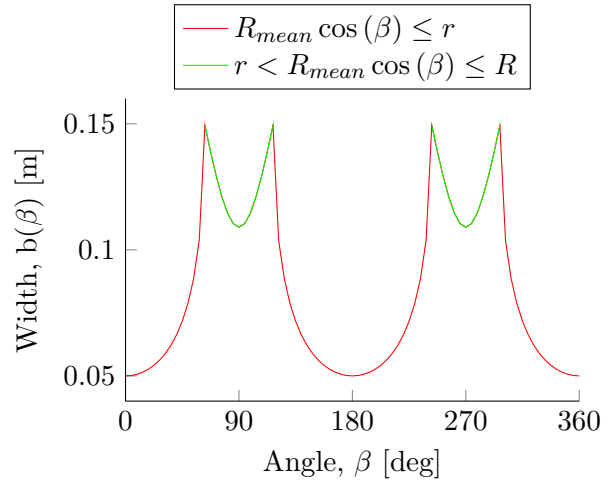


**Figure 2.6** The width,  $b(\beta)$ , is plotted as a function of the angle  $\beta$ . The red curve is the first part of the piece-wise function in equation (2.32) and the green curve is the second part. The nomenclature and colours are illustrated in figure 2.5.

## 2.5 Jacket model

The jacket support structure is modelled with 108 elements. All elements are assumed to be perfectly welded together, by which they transfer force and moment loads at the nodes. The model is shown in figure 2.7, where the red spots are the four nodes (1, 6, 11, 16) which are fixed in all DOF's. This does not take the stiffness of the piles, which is hammered into the seabed, into account. Since this is the location with the greatest bending moment, it may have an compliant influence of the global response of the jacket structure due to the piles being independent of each other. However, it is assessed that by fixing the nodes at the seabed, it will yield reasonable results with respect to the global response and estimation of fatigue of the jacket structure. The loads, which are presented in section 2.5.1, are applied at node 57 (pink dot). Although, the loads from the wind turbine tower would be applied over a greater area, it is assessed that by increasing the stiffness of the nearby elements, the loads will be distributed in a decent manner, as described below.

The cross-sectional parameters of the UpWind jacket structure are shown in figure 2.8. The following material data is used for all elements in the model: Young's modulus of 210 GPa, Poisson's ratio of 0.3, and density of 7800 kg/m<sup>3</sup>. However, the green lines are the elements (101-108) which have a 100 times larger Young's modulus than the other elements. This ensures that the applied loads are distributed to the whole structure. These elements are also cast into the transition piece, as described in chapter 1, and therefore the cross-sectional data of these elements remain unchanged during the optimisation. The cross-section of each element is modelled as a uniform circular tube, where the cross-sectional data does not change along the length of the element. Although there will be overlapping cross-sections near the joint of multiple elements.

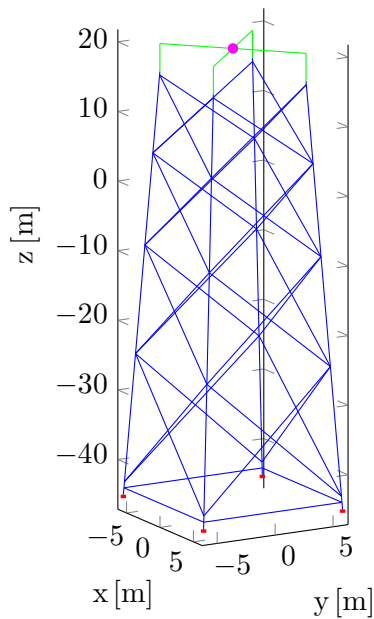


**Figure 2.7** Sketch of jacket model with boundary and load conditions.

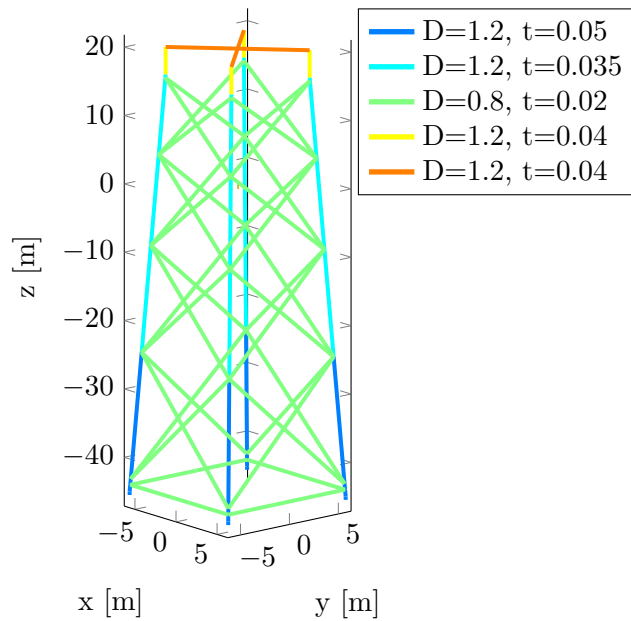


**Figure 2.8** Initial sections of the UpWind jacket structure. The color of the element represent sectional dimensions in meters, which is seen in the legend box.

### 2.5.1 Loading history

In order to simplify the model, only resulting loads from a simulation of a wind turbine tower are applied. The HAWC2 program from the Risø National Laboratory has been used to perform a 600 s simulation of a Wind turbine. It is DTU Wind Energy Group who has performed the simulation and provided the resulting forces at the bottom of the wind turbine tower.[Jørgensen and Nissen, 2013] This is obvious because the jacket structure is submerged in the sea, by which wave loads should be considered. However, these loads have been neglected, in order to develop a simple linear model.

The applied wind speeds in the HAWC2 simulation are shown in figure 2.9. However, the applied wind speeds are assessed as the normal wind conditions, since no extreme wind speeds have been included in the simulation. The estimated fatigue life of the jacket structure is based on the loading from these wind speeds and therefore it should be considered if it is necessary to include more load cases in order to represent the real loading conditions. However, this is not considered in this project, but it could be included in the optimisation problem and written as a multi objective problem.

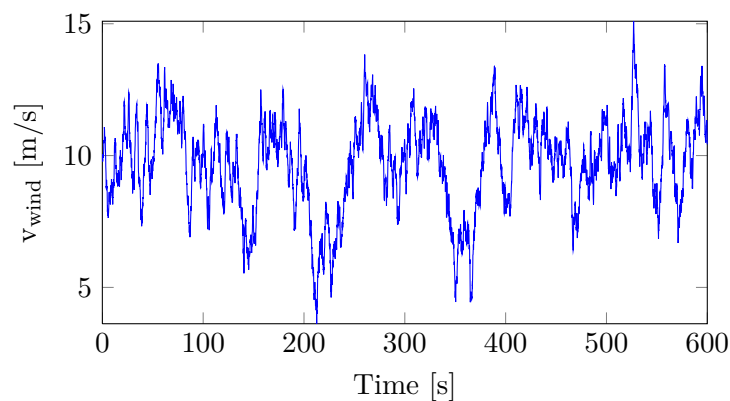


**Figure 2.9** Applied wind speed in the HAWC2 simulation.

The loading history is shown in figure 2.10. It is nonproportional, since the components vary out-of-phase. The concept of nonproportional loading is described in section 4.1. The resulting vertical force,  $F_z$ , and the moment about the vertical axis,  $M_z$ , have not been available. However, it would be possible to estimate the mass of the wind turbine and apply it as a static vertical load, but since it is a linear FEM which is performed, this would contribute an equal amount at all loading conditions. Although, the compressive load may lead to compressive stresses in some of the elements, which does have a beneficial effect on the fatigue life. In the analysis of the jacket structure the loadings shown in figure 2.10 are applied. The loads are applied at node 57 (pink dot in figure 2.7).

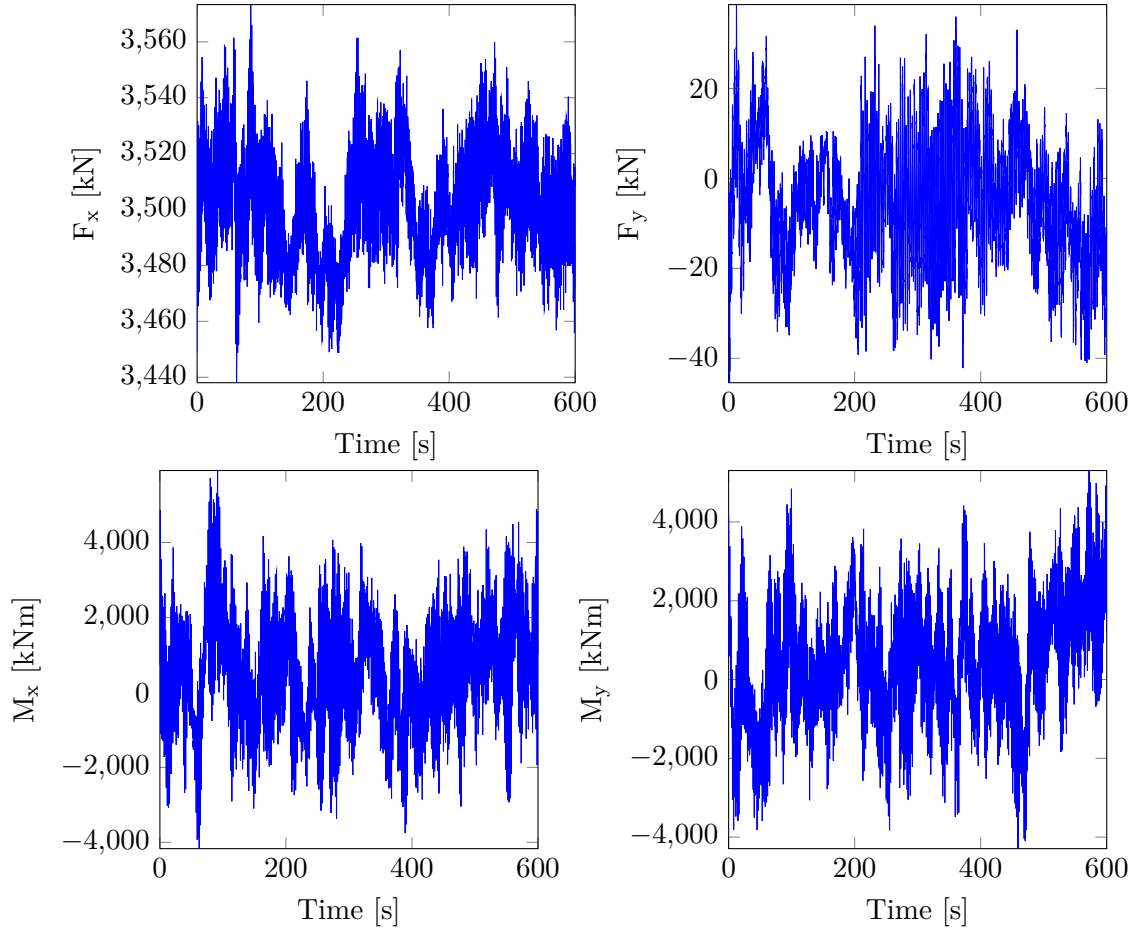


**Figure 2.10** Applied load history at TP of jacket structure.

The load history is sampled at 100 Hz, by which the load components contain 60,000 samples each. In order to reduce the computational time, since the displacements of the jacket structure would have to be evaluated for each sample, the loading history is reduced. Jørgensen and Nissen [2013] reduced the size of load history by only including the turning point samples. However if this is applied to the loading components individually, the turning points of each load component may not be at the same time-samples. Therefore, the load history is reduced by searching for turning points in an equivalent load history, which is seen in equation (2.33).

$$F_{eq} = \sqrt{F_x^2 + F_y^2 + F_z^2 + M_x^2 + M_y^2 + M_z^2} \quad (2.33)$$

The load history is reduced from 60,000 samples to 3,032 samples by only including the turning points found in the equivalent load history,  $F_{eq}$ .

A 10 s segment of the equivalent load history (blue) is seen in the left-hand graph in figure 2.11, along with the reduced equivalent load history (red). It is clear that the reduced load history only includes the turning point samples. The right-hand side of the figure, shows the force in the x-direction, where a 10 s segment of the full load history is compared with the reduced load history. Most of the small spikes from the full load history have been removed from the reduced load history, although the extreme spikes have not been preserved in the reduced load history. This is because the reduction is conducted for the equivalent load history.



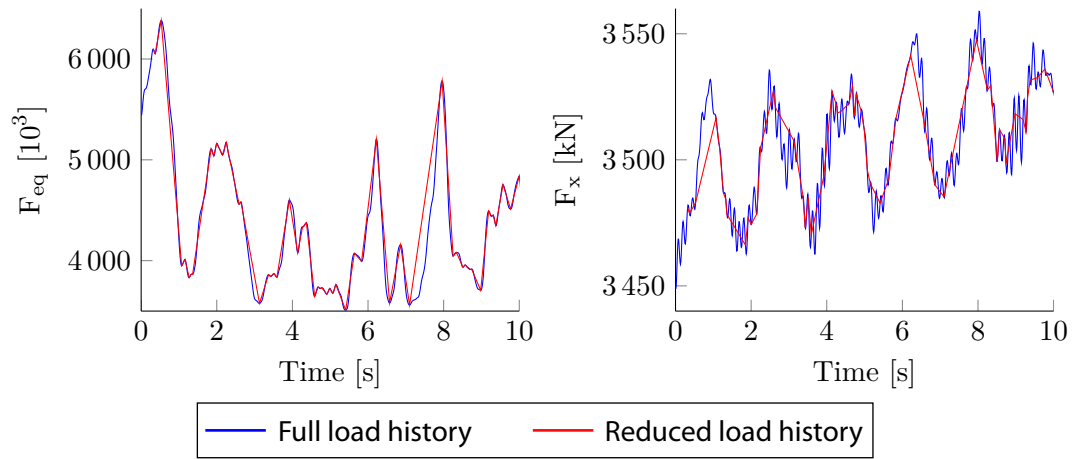


**Figure 2.11** Comparison of full and reduced load history. Left: 10 s segment of the equivalent load history,  $F_{eq}$ . Right: 10 s segment of the load,  $F_x$ .



# Verification of FEM code

# 3

In this chapter the FEM code written in MATLAB is verified. The model of the jacket structure, presented in chapter 1, is used during the verification. The MATLAB code is compared with an ANSYS model, which uses an element stiffness matrix that is derived for the Timoshenko beam element, whereas the MATLAB FE code is based on a Bernoulli-Euler beam element. The mass matrix for both models are identical. Even though the element stiffness matrices are not the same, it is assessed that, due to the long and slender beams, it will not produce major differences in the results. In appendix A is the ANSYS model described, including a description of the utilised element, BEAM188. In the preceding sections, the jacket structure is evaluated w.r.t. natural frequency and global displacement. The verification of stress calculation is done with a simpler structure that consists of two elements, as described in section 3.3.

## 3.1 Natural frequency

In this analysis the jacket model, described in section 2.5, is used but with no loads applied. The natural frequency of the jacket structure is obtained by the eigenvalue problem in equation (3.1). The nontrivial solution is that the expression in the parenthesis must be equal to zero. By taking the determinant of the expression in the parenthesis and equating it to zero, the eigenvalues  $\lambda$  is found.

$$([K] - \lambda_i [M]) \{D_i\} = \{0\} \quad \text{where} \quad \lambda_i = \omega_i^2 \quad (3.1)$$

where:

[Cook et al., 2001, p. 378]

|             |                                  |
|-------------|----------------------------------|
| $[K]$       | Global stiffness matrix, [-]     |
| $[M]$       | Global mass matrix, [-]          |
| $\{D_i\}$   | Mode shape, [-]                  |
| $\lambda_i$ | Eigenvalue, $[(\text{rad/s})^2]$ |
| $\omega_i$  | Natural frequency, [rad/s]       |

When the eigenvalues,  $\lambda_i$ , and thereby the natural frequencies,  $\omega_i$ , are known, the associated mode shapes,  $\{D_i\}$ , can be determined. For each natural frequency, a corresponding mode shape exists. The mode shape is determined by solving equation (3.1) w.r.t.  $\{D_i\}$  for the current natural frequency,  $\omega_i$ . The vector  $\{D_i\}$  is the mode shape which describes the configuration of the jacket structure for the corresponding natural frequency,  $\omega_i$ .

In the analysis of the jacket structure, a consistent mass matrix is used. The consistent mass matrix, which is shown in equation (3.2), has the same form as the element stiffness matrix and thereby includes dynamic couplings between translations and rotations. If a lumped mass matrix was used, only the translational DOF of the diagonal will be included. The eigenvalue problem in equation (3.1) is faster to solve, when using the lumped mass matrix, however since

the natural frequencies are only used as a verification the calculation time is not considered.

$$[{}_lM_e] = \rho A_e L_e \begin{bmatrix} X & 0 & 0 & 0 & 0 & 0 & 2X & 0 & 0 & 0 & 0 & 0 \\ & Z_1 & 0 & 0 & 0 & Z_2 & 0 & Z_4 & 0 & 0 & 0 & -Z_5 \\ & & Y_1 & 0 & -Y_2 & 0 & 0 & 0 & Y_4 & 0 & Y_5 & 0 \\ & & & 2S & 0 & 0 & 0 & 0 & 0 & S & 0 & 0 \\ & & & & Y_3 & 0 & 0 & 0 & -Y_5 & 0 & Y_6 & 0 \\ & & & & & Z_3 & 0 & Z_5 & 0 & 0 & 0 & Z_6 \\ & & & & & & X & 0 & 0 & 0 & 0 & 0 \\ & & & & & & & Z_1 & 0 & 0 & 0 & -Z_2 \\ & & & & & & & & Y_1 & 0 & Y_2 & 0 \\ & & & & & & & & & 2S & 0 & 0 \\ & & & & & & & & & & Y_3 & 0 \\ & & & & & & & & & & & Z_3 \end{bmatrix} \quad (3.2)$$

where  $[{}_lM_e]$  is the element stiffness matrix and  $X$ ,  $S$ ,  $Y_i$ , and  $Z_i$  are defined as:

$$\begin{aligned} X &= \frac{1}{3} & S &= \frac{J_x}{6 A_e} \\ Y_1 &= \frac{13}{35} + \frac{6 I_y}{5 A_e L_e^2} & Z_1 &= \frac{13}{35} + \frac{6 I_z}{5 A_e L_e^2} \\ Y_2 &= \frac{11 L_e}{210} + \frac{I_y}{10 A_e L_e} & Z_2 &= \frac{11 L_e}{210} + \frac{I_z}{10 A_e L_e} \\ Y_3 &= \frac{L_e^2}{105} + \frac{2 I_y}{15 A_e} & Z_3 &= \frac{L_e^2}{105} + \frac{2 I_z}{15 A_e} \\ Y_4 &= \frac{9}{70} - \frac{6 I_y}{5 A_e L_e^2} & Z_4 &= \frac{9}{70} - \frac{6 I_y}{5 A_e L_e^2} \\ Y_5 &= \frac{13 L_e}{420} - \frac{I_y}{10 A_e L_e} & Z_5 &= \frac{13 L_e}{420} - \frac{I_z}{10 A_e L_e} \\ Y_6 &= -\frac{L_e^2}{140} - \frac{I_y}{30 A_e} & Z_6 &= -\frac{L_e^2}{140} - \frac{I_z}{30 A_e} \end{aligned} \quad (3.3)$$

where:

|       |   |
|-------|---|
| $A_e$ | Cross-sectional area of element, $[\text{m}^2]$           |
| $L_e$ | Length of the element, $[\text{m}]$                       |
| $I_y$ | Area moment of inertia w.r.t. the y-axis, $[\text{m}^4]$  |
| $I_z$ | Area moment of inertia w.r.t. the z-axis, $[\text{m}^4]$  |
| $J_x$ | Polar moment of inertia w.r.t. the x-axis, $[\text{m}^4]$ |

[Przemieniecki, 2012]

The assembly of the global mass matrix,  $[M]$ , is similar to the assembly of the global stiffness matrix, which is described in section 2.2.

In table 3.1, the first ten natural frequencies are presented and compared with the ANSYS model. The two lowest natural frequencies shows good correlation between the two models, which are bending modes of the structure. Afterwards, there are a deviation of about 3% between the two models. The mode shape of these natural frequencies have more local effects, which may be estimated better with the Timoshenko stiffness matrix that takes shear deformation into account. The ability to deform in shear will take more energy of the system, by which lowering the natural frequency, as seen in the table. The mode shapes are the same in both MATLAB and ANSYS for all ten natural frequencies.

| Number | MATLAB<br>[Hz] | ANSYS<br>[Hz] | Difference<br>[%] | Mode shape   |
|--------|----------------|---------------|-------------------|--|
| 1      | 2.618          | 2.6122        | 0.22              | Bending about y                                    |
| 2      | 2.618          | 2.6122        | 0.22              | Bending about x                                    |
| 3      | 5.7169         | 5.6349        | 1.4               | Twisting about z                                   |
| 4      | 8.1591         | 7.9332        | 2.8               | Bending about y with local out-of-plane deflection |
| 5      | 8.1591         | 7.9332        | 2.8               | Bending about x with local out-of-plane deflection |
| 6      | 8.9475         | 8.614         | 3.7               | Diagonal warping                                   |
| 7      | 9.3638         | 9.0858        | 3                 | Local out-of-plane deflection 1                    |
| 8      | 9.9389         | 9.5566        | 3.8               | Local out-of-plane deflection 1                    |
| 9      | 10.24          | 9.9098        | 3.2               | Local out-of-plane deflection 2                    |
| 10     | 10.24          | 9.9098        | 3.2               | Local out-of-plane deflection 2                    |

**Table 3.1** Comparison of natural frequencies calculated by ANSYS and the MATLAB code.

## 3.2 Global displacement

The global displacements are calculated by the MATLAB code and compared with the ANSYS model. The displacements of the nodes at  $z = 20.15$  m, according to figure 2.7, are compared in table 3.2. The jacket structure is applied force and moment loads at node 57 of; 10 kN in the x, y, and z direction and 10 kNm about the x, y, and z axes. The differences in the displacements are small. It is likely caused by the different element stiffness matrix used in the ANSYS model, which uses a Timoshenko beam element, as described in appendix A, whereas a Bernoulli-Euler beam element is used in the MATLAB code. It is assessed that the results produced by the MATLAB code, w.r.t. displacements, are valid.

| Node | Type        | u<br>[mm] | v<br>[mm] | w<br>[mm] | 3-Norm | Difference<br>[%] |
|------|-------------|-----------|-----------|-----------|--------|-------------------|
| 53   | MATLAB code | 0.268     | 0.271     | -0.0417   | 0.384  | 1.6               |
|      | ANSYS       | 0.267     | 0.264     | -0.0416   | 0.378  |                   |
| 54   | MATLAB code | 0.268     | 0.257     | 0.00668   | 0.371  | 0.71              |
|      | ANSYS       | 0.266     | 0.255     | 0.0067    | 0.369  |                   |
| 55   | MATLAB code | 0.283     | 0.271     | 0.00323   | 0.392  | 2.5               |
|      | ANSYS       | 0.276     | 0.264     | 0.00324   | 0.382  |                   |
| 56   | MATLAB code | 0.283     | 0.257     | 0.0516    | 0.385  | 1.6               |
|      | ANSYS       | 0.276     | 0.255     | 0.0515    | 0.379  |                   |
| 57   | MATLAB code | 0.276     | 0.264     | 0.00524   | 0.382  | 1.6               |
|      | ANSYS       | 0.271     | 0.26      | 0.00528   | 0.376  |                   |

**Table 3.2** Comparison of global displacements calculated by ANSYS and the MATLAB code.

### 3.3 Stress

The stresses around the cross-section of an element is evaluated and a comparison between the MATLAB FE model and an ANSYS model is conducted. The model is shown in figure 3.1, where the local coordinate system of the two elements are shown in figure 3.2. Each element in the model is 1 m and is perpendicular to each other. Node 1 coincides with origo in the global coordinate system and is fixed in all DOF's. The results are presented according to the local coordinate system and the angle,  $\beta$ , is according to figure 2.4. The stresses in the MATLAB model is evaluated at the mean radius, whereas the ANSYS stresses are the average of the stress at the outside and inside of the tube, e.g. node 1 and 2 in figure A.1. Each element has been modelled with the following cross-sectional and material datas: outer diameter of 50 mm, wall thickness of 5 mm, Young's modulus of 210 GPa, and Poisson's ratio of 0.3.

The internal forces, for each element, have been compared and showed no difference between MATLAB and ANSYS. These results are not shown below.

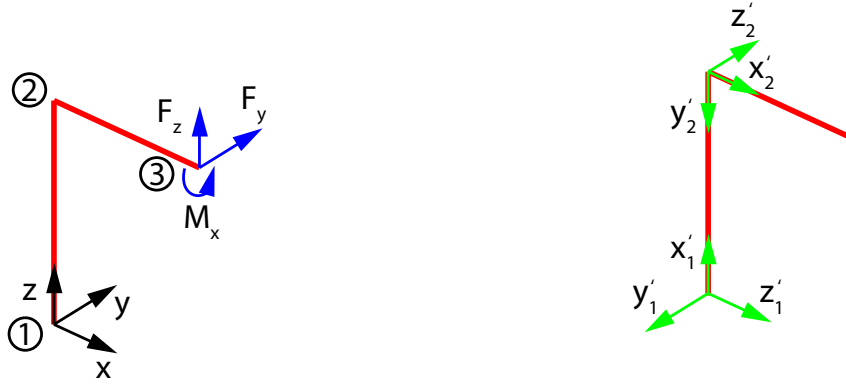


**Figure 3.1** Simple 3D beam model with two elements, three nodes and it is fixed at origo.

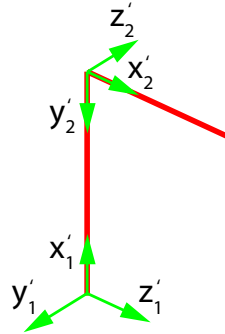


**Figure 3.2** The local coordinate system of the two elements are the green  $x'$ - $y'$ - $z'$  coordinate systems.

#### 3.3.1 Normal stress

The normal stresses are compared at node 2 in element 2, where a shear force of  $F_y = 1000$  N is applied, according to figure 3.1. The results are shown for a cross-sectional division of 8, this is the minimum allowed number of section divisions in ANSYS.

There is a negligible difference between the normal stresses in the cross-section calculated by ANSYS and the MATLAB FEM. The difference decreases with increasing number of section divisions and it is not influenced by multiaxial loads.

|                | Element 2, node 2 |        |        |        |     |        |        |        |
|----------------|-------------------|--------|--------|--------|-----|--------|--------|--------|
| $\beta$ [deg]  | 0                 | 45     | 90     | 135    | 180 | 225    | 270    | 315    |
| MATLAB [MPa]   | 0                 | -87.8  | -124   | -87.8  | 0   | 87.8   | 124    | 87.8   |
| ANSYS [MPa]    | 0                 | -88    | -124   | -88    | 0   | 88     | 124    | 88     |
| Difference [%] | 0                 | -0.207 | -0.207 | -0.207 | 0   | -0.207 | -0.207 | -0.207 |

**Table 3.3** Normal stress in cross-section by ANSYS and the MATLAB model. Normal stresses as a function of angle  $\beta$  for node 2 in element 2.

### 3.3.2 Shear stress

The comparison of the shear stresses are conducted for three load cases, where the loads, in the following, are applied according to figure 3.1.

**Load case 1:** Shear force of  $F_z = 1000$  N

**Load case 2:** Torque of  $M_x = 1000$  Nm

**Load case 3:** Shear force of  $F_z = 1000$  N and  $F_y = 1000$  N

The results for each load case is presented in figure 3.3 to 3.5, where the shear stress in node 2 of element 2 is plotted as a function of the angle  $\beta$  in figure 2.4. For all load cases a cross-sectional division of 80 is used.

#### Load case 1

The MATLAB xz shear stress variation in the cross-section is consistent with the ANSYS xz shear stress, as shown in figure 3.3. Since only a shear force in  $F_z$  is applied there should not be any stresses in xy, but somehow ANSYS calculates a variation in the xy shear stress. The xy shear stress by ANSYS has a phase-shift of  $45^\circ$  and oscillates about the stress level of 0 MPa with an amplitude of exactly half the maximum value of the xz shear stress. The reason for this has not been available in ANSYS [2011].

The non-continuity of the xz shear stress at approximately  $60^\circ$  to  $120^\circ$  is caused by the width  $b(\beta)$ , used in equation (2.28), which is a piece-wise function due to the hollow circular cross-section. The non-continuity is only noticeable with a large number of cross-sectional divisions and therefore the deviation is assessed to be negligible.

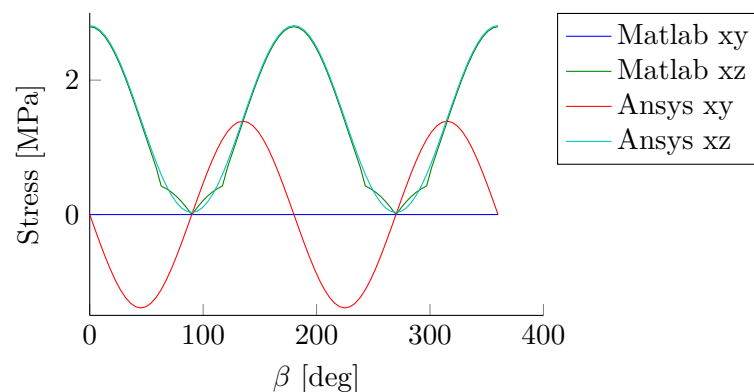


**Figure 3.3** Shear stress as a function of the angle  $\beta$  shown in figure 2.4. A shear force of  $F_z = 1000$  N is applied according to figure 3.1, and stresses are shown for node 2 in element 2.

#### Load case 2

The shear stresses from pure torque are shown in figure 3.4. There is no difference between the shear stresses calculated by MATLAB or ANSYS, by which the torsional related shear stress calculation is verified.

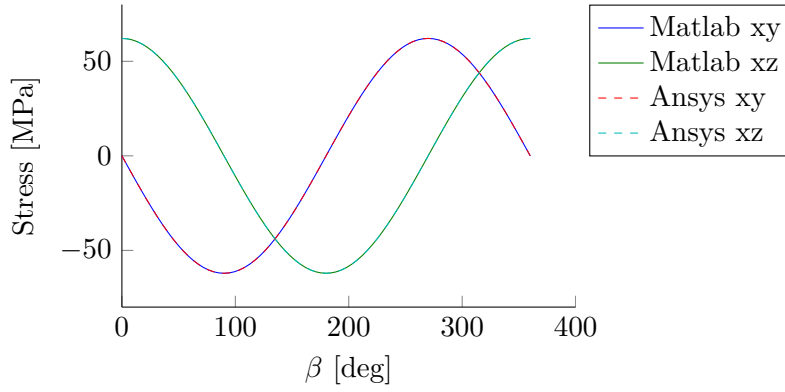


**Figure 3.4** Shear stress as a function of the angle  $\beta$  shown in figure 2.4. A moment of  $M_x = 1000 \text{ Nm}$  is applied according to figure 3.1, and stresses are shown for node 2 in element 2.

### Load case 3

The third load case is biaxial, but since the model is linear elastic, the principle of superposition is valid and the shear stress contribution can be separated. The results from ANSYS have a phase-shift compared with MATLAB and the amplitudes are higher, whether this is due to the oscillating shear stress in load case 1 is not clear. This disagreement in shear stresses may be investigated further, but since the MATLAB FE model is able to calculate the correct displacements, natural frequencies, and normal stresses, this has been omitted.

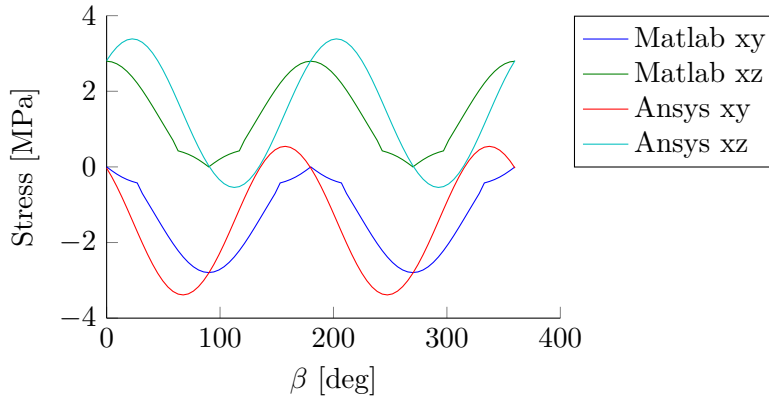


**Figure 3.5** Shear stress as a function of the angle  $\beta$  shown in figure 2.4. A shear force of  $F_z = 1000 \text{ N}$  and  $F_y = 1000 \text{ N}$  is applied according to figure 3.1, and stresses are shown for node 2 in element 2.



# Fatigue 4

---

This chapter describes the methods which are used to perform the fatigue analysis of the jacket structure. The nonproportional loading of the beam elements is handled with use of a multiaxial rainflow counting method, presented in section 4.2, which counts the mean- and alternating stress reversals. The fatigue life is estimated using a multiaxial fatigue model by Findley, described in section 4.3 which is able to handle nonproportional loading, as well. The applied loading history, which is utilised in the fatigue analysis, is described in section 2.5.1.

## 4.1 Proportional and Nonproportional loading

When selecting a fatigue model, it is necessary to identify the loading type. Two types of loading are considered, proportional and nonproportional. They are described by considering a uniform bar which is applied a force,  $P$ , and a torque,  $T$ , as shown in figure 4.1. The stress components in the element on the circumference of the uniform bar are plotted as a function of time in figure 4.2. If the force and torque are applied in-phase such that the maximum and minimum normal and shear stress occur simultaneously, then the loading type is considered as proportional. Whereas, if the force and torque are applied out-of-phase then the loading type is considered as nonproportional. The proportional and nonproportional loadings are shown in figure 4.2b and 4.2d, respectively. [Stephens et al., 2001]

The proportional loading is often present in simple and controlled loading conditions, e.g. a shock absorber, torque applied by a screw driver, or a forced vibrating beam clamped at the end. Several fatigue models are applicable with proportional loading, also multiaxial, e.g. S-N and  $\epsilon$ -N approach which estimate the fatigue life using stresses and strains, respectively. The fatigue life parameters are mostly estimated by empirical data, e.g. Wöhler curves are conducted from multiple cyclic bending tests, which is a proportional loading condition.

The nonproportional loading is due to complicated loading conditions, where multiple loads are applied out-of-phase. An example, besides the jacket structure, is a spinning wheel of a driving car. If the wheel is not perfectly balanced, this will cause the wheel to vibrate. The vibrations produce strains and thereby stresses in the wheel. The stresses from the vibration may not be in-phase with the varying load of the spinning wheel, due to the load of the car.

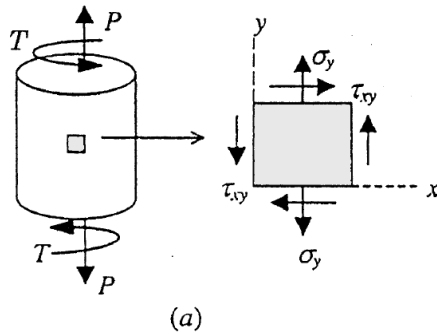


**Figure 4.1** Uniform bar with applied force,  $P$ , and torque,  $T$ . The gray square is the stress element for which the stresses are plotted in figure 4.1. [Stephens et al., 2001, p. 321]

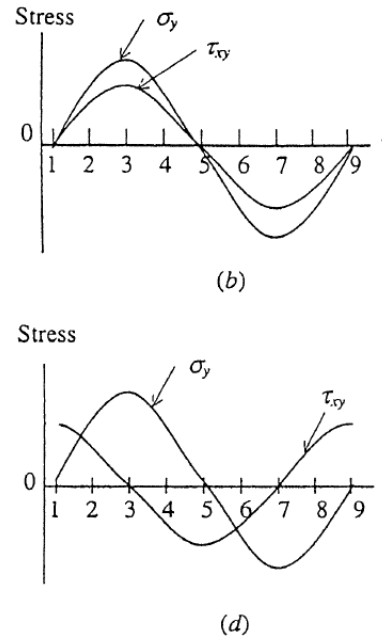


**Figure 4.2** Stresses in the stress element as a function of time where (b) is proportional loading and (d) is nonproportional loading. [Stephens et al., 2001, p. 321]

The loads applied to the jacket structure, which is shown in section 2.5.1, are multiaxial and nonproportional. Therefore, a counting method and fatigue model, which is able to handle multiaxial nonproportional loading is needed. In the next section, the counting method is assessed.

## 4.2 Counting method for nonproportional loading

This section presents the counting method, which is used to count the reversals from the load history. A commonly used method for variable amplitude loading is the rainflow counting method described by Stephens et al. [2001, p. 282]. This method identifies the reversals as being from a valley to the most distant peak, which does not intersect with an already counted reversal. By which each load range of a reversal is from the valley to the peak load. However, the traditional rainflow counting method is only applicable for proportional uniaxial loading conditions since only the load history in one direction is accounted for during the rainflow count. By which the peak or valley of the load history in one direction may not coincide with the corresponding load history in another direction.

One of the methods, suggested by Stephens et al. [2001], for dealing with multiaxial nonproportional variable amplitude loading is the method by Wang and Brown [1996], which is counting cycles based on an equivalent strain, such as the Mises strain,  $\varepsilon_{Mises}$ . Meggiolaro and de Castro [2011b] emphasise the drawback of using the equivalent strain due to the loss of loading event sign, since the equivalent strain is always positive. Therefore, the modified Wang-Brown model by Meggiolaro and de Castro [2011b] is used.

The Modified Wang-Brown (MWB) method applies a five dimensional, either stress or strain,

subspace. In the FE model, the stress subspace is used. The multiaxial stress history is represented by a series of points in the 5D subspace,  $P_i = (S_1, S_2, S_3, S_4, S_5)$ , where  $S_i$  is given in equation (4.1). The expressions for the strain subspace is given in equation (4.2). The MWB method also works in a lower dimensional subspace, e.g.  $P_i = (S_1, S_3)$ .

$$\begin{aligned} S_1 &= \sigma_x - \frac{\sigma_y}{2} - \frac{\sigma_z}{2}, & S_2 &= \frac{\sigma_y - \sigma_z}{2} \sqrt{3} \\ S_3 &= \tau_{xy} \sqrt{3}, & S_4 &= \tau_{xz} \sqrt{3}, & S_5 &= \tau_{yz} \sqrt{3} \end{aligned} \quad (4.1)$$

$$\begin{aligned} e_1 &= \frac{2\varepsilon_x - \varepsilon_y - \varepsilon_z}{2(1+\bar{\nu})}, & e_2 &= \frac{\varepsilon_y - \varepsilon_z}{2(1+\bar{\nu})} \sqrt{3} \\ e_3 &= \frac{\gamma_{xy}}{2(1+\bar{\nu})} \sqrt{3}, & e_4 &= \frac{\gamma_{xz}}{2(1+\bar{\nu})} \sqrt{3}, & e_5 &= \frac{\gamma_{yz}}{2(1+\bar{\nu})} \sqrt{3} \end{aligned} \quad (4.2)$$

where:

[Meggiolaro and de Castro, 2011b]

|             |   |
|-------------|---|
| $\sigma_i$  | Normal stress w.r.t. the $i^{\text{th}}$ axis, [Pa] |
| $\tau_{ij}$ | Shear stress w.r.t. the $ij$ plane, [Pa]            |
| $\bar{\nu}$ | Effective poisson's ratio,, [-]                     |

This results in a stress history represented as a cloud of points in a, up to, 5D space. The distance between each point, in the 5D space, is used when searching for the cycles. This way the nonproportionality is taken into account.

The MWB algorithm is initialised by reordering the load history. It is conducted by first finding point pairs which form the longest chord in the 5D subspace and secondly choosing the point, among the point pairs, which has the greatest distance from the origin. This point is the first point,  $P_1$ , of the reordered load history. The subsequent point should follow the original order of the load history and end with a copy of the first point. Each count sequentially starts at  $P_1, P_2, \dots, P_i, \dots, P_n$ . The count should only be terminated if the current point is farthest away from the start point or if it intersects with an already counted segment.

The MWB algorithm is explained by the following example, which is used in Meggiolaro and de Castro [2011b]. For the given example, the MWB algorithm has already been initiated, by which the load history is reordered. The reordered load history is represented in a 2D subspace,  $[P_1, \dots, P_7]$  where  $P_7 = P_1$ . The numeric values of each points are not important in this example. The load history is load block from a cyclic tension-torsion test. The loading order is sorted alphabetically from A to F, where the strain values are given in table 4.1.

|               | A | B  | C | D  | E  | F  |
|---------------|---|----|---|----|----|----|
| $\varepsilon$ | 2 | -2 | 2 | -1 | 2  | -2 |
| $\gamma$      | 2 | 0  | 1 | 2  | -2 | -2 |

**Table 4.1** Cyclic tension-torsion load history in % strain.

The load history table 4.1 is mapped into the subspace by defining  $\varepsilon = \varepsilon_x$  and  $\gamma = \gamma_{xy}$ , assuming that  $\varepsilon_y = -\bar{\nu} \varepsilon_x$ ,  $\varepsilon_z = -\bar{\nu} \varepsilon_x$ , and an effective Poissons ratio of 0.4. By which the load history is represented in the subspace as  $P_i = (e_1, e_3)$ , which is shown in table 4.2.

|       | $P_1$ | $P_2$ | $P_3$ | $P_4$ | $P_5$ | $P_6$ | $P_7$ |
|-------|-------|-------|-------|-------|-------|-------|-------|
| $e_1$ | 2     | -2    | 2     | -1    | 2     | -2    | 2     |
| $e_3$ | 1.24  | 0     | 0.619 | 1.24  | -1.24 | -1.24 | 1.24  |

**Table 4.2** Load history from table 4.1 represented in the  $e_1$ - $e_3$  subspace in % strain.

A  $\gamma$ - $\varepsilon$  diagram of the load history in table 4.1 is shown in figure 4.3, together with the corresponding path in the 2D subspace from table 4.2. The counting of the paths are shown in figure 4.4 to 4.9, where the red dashed lines are the path which has been counted during the given count and the solid blue lines are paths which has already been counted.

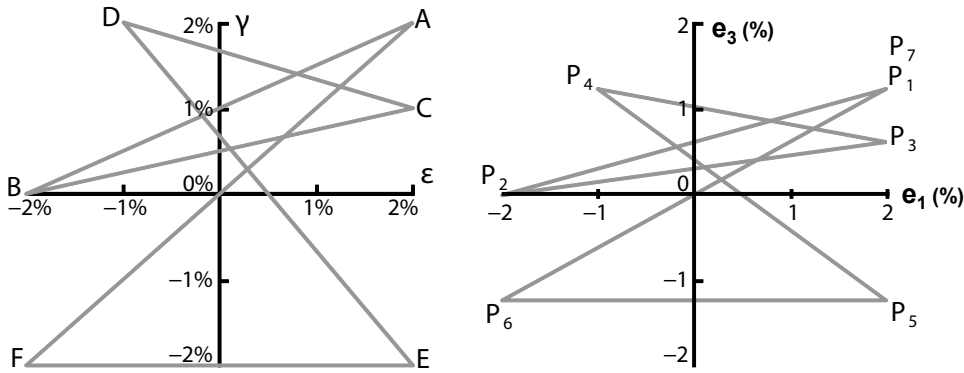


**Figure 4.3** Left:  $\gamma$ - $\varepsilon$  diagram of nonproportional load history. Right: Corresponding path in the 2D subspace. [Meggiolaro and de Castro, 2011b]

The first count starts at  $P_1$ , as shown in figure 4.4. It uses the entire segment  $P_1$ - $P_2$  and the only point which is further away from  $P_1$  than  $P_2$  is  $P_6$ , by which  $P_2$  is projected onto the  $P_5$ - $P_6$  segment. The projection onto  $P_5$ - $P_6$  is  $P'_5$ , which is an equal amount away from  $P_1$  as  $P_2$ . The count continues to  $P_6$ , which is the point most distant from  $P_1$ , and terminates.

The second count starts at  $P_2$ , as shown in figure 4.5. It uses the entire segment  $P_2$ - $P_3$ . Since  $P_5$  is more distant from  $P_2$  than  $P_3$ ,  $P_3$  is projected onto segment  $P_4$ - $P_5$ , which introduces  $P'_4$ . Count continues to  $P_5$ , but since  $P_5$  and  $P_7$  are equally away from  $P_2$ , this count terminates at  $P_7$ .

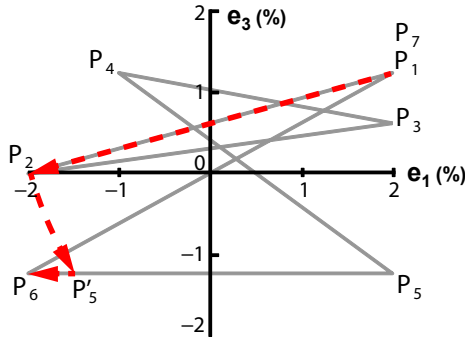


**Figure 4.4** 2D subspace diagram of first count.

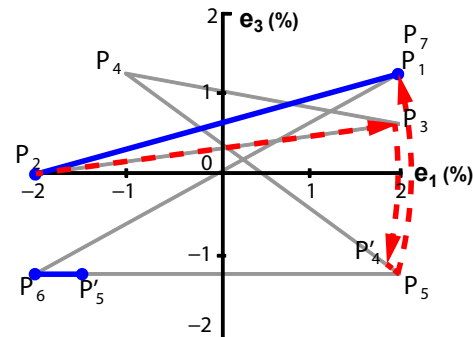


**Figure 4.5** 2D subspace diagram of second count.

The third count starts at  $P_3$ , as shown in figure 4.6. It uses the entire segment  $P_3$ - $P_4$ . Since  $P_6$  is the most distant point from  $P_3$  than  $P_4$ ,  $P_4$  is projected onto segment  $P_5$ - $P_6$ , which introduces  $P''_5$ . This count terminates at  $P'_5$ , since  $P'_5$ - $P_6$  has already been counted.

The fourth count starts at  $P_4$ , as shown in figure 4.7. It terminates at  $P'_4$ , since  $P'_4$ - $P_5$  has already been counted.

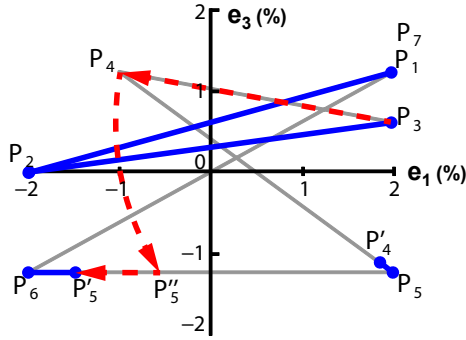


**Figure 4.6** 2D subspace diagram of third count.

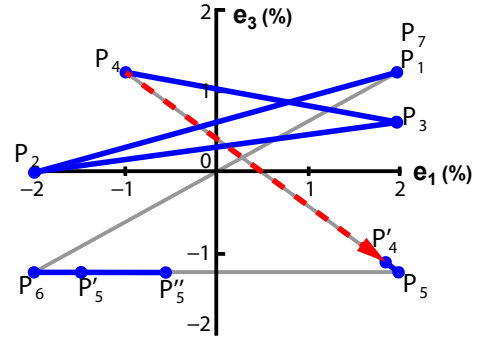


**Figure 4.7** 2D subspace diagram of fourth count.

The fifth count starts at  $P_5$ , as shown in figure 4.8. It terminates at  $P''_5$ , since  $P''_5$ - $P'_5$  and  $P'_5$ - $P_6$  have already been counted.

The sixth and final count starts at  $P_6$ , as shown in figure 4.9. It terminates at  $P_7$ , since this is the last point of the 2D subspace.

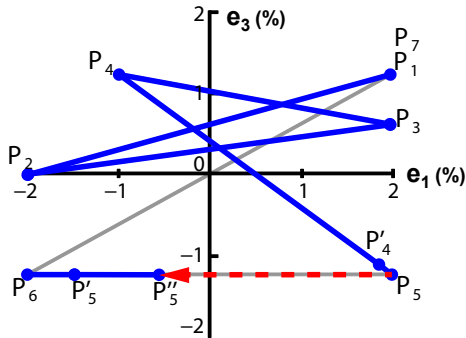


**Figure 4.8** 2D subspace diagram of fifth count.

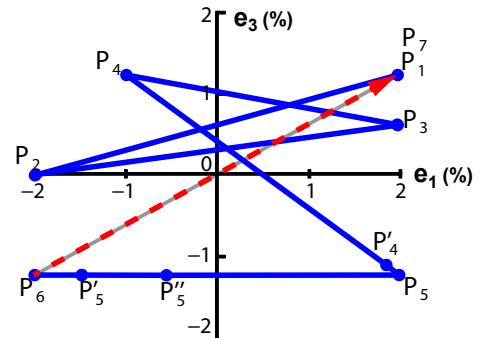


**Figure 4.9** 2D subspace diagram of sixth count.

When the MWB algorithm terminates the entire load history has been counted, by which the resulting reversals are shown in figure 4.10. The counted reversals are afterwards applied in the assessment of the fatigue damage done by this load history.

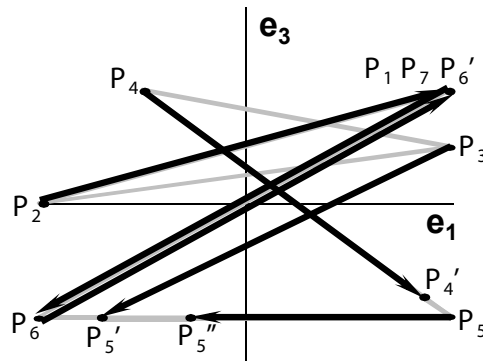


**Figure 4.10** 2D subspace diagram of the MWB count, where arrows represent reversals. [Meggiolaro and de Castro, 2011b]

The MWB algorithm has not, in this project, been compared with any other counting methods. However, it has been implemented in the MATLAB code and verified by the example in Meggiolaro and de Castro [2011b]. Due to introduction of the 5D subspace, this counting method is capable of handling both proportional and nonproportional loading history with varying amplitudes while preserving the load order.

#### 4.2.1 Mean and alternating components

Fatigue models are often based on stress or strain ranges in order to estimate the fatigue life. For proportional constant amplitude loading these ranges can be calculated from the peak and valley values, which may be found using the traditional rainflow counting method. However, for more complex loading conditions, such as nonproportional variable amplitude loading, the path of the counted reversal has to be considered. When the load path of a reversal consists of more than two load points, e.g. the counted reversal defined by the segment  $P_1 - P_2 - P'_5 - P_6$  in figure 4.4, it may not be apparent how to determine the effective stress or strain ranges of the reversal.

In Meggiolaro and de Castro [2011a] several methods are described in order to determine the effective stress ranges. Two of the enclosing surface methods are the minimum ball and the minimum volume ellipsoid, which is applied to the  $P_1 - P_2 - P'_5 - P_6$  segment in figure 4.11. The  $P_1 - P_2 - P'_5 - P_6$  segment is given in the deviatoric strain space, equivalent to the stress subspace in equation (4.1). It is assumed that the deviatoric stress range,  $\Delta S$ , is equal to the effective Von Mises stress range,  $\Delta\sigma_{Mises}$ , by which the diameter of the minimum ball and the norm of the semi-axis of the minimum volume ellipsoid are the effective Von Mises strain ranges. These enclosing surface methods do not determine the stress or strain ranges accurately when used with nonproportional loading, by which the Moment Of Inertia (MOI) method is suggested. [Meggiolaro and de Castro, 2011a]

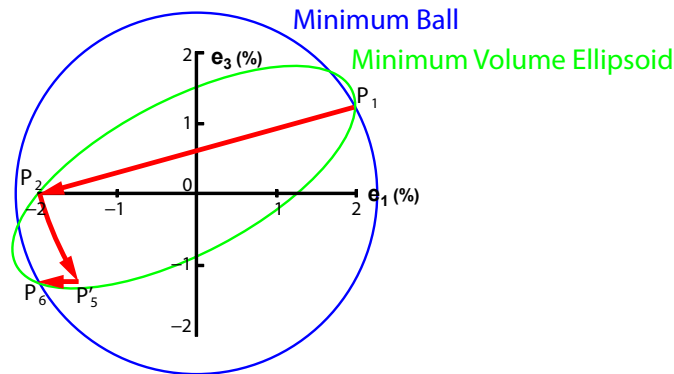


**Figure 4.11** Load segment  $P_1 - P_2 - P'_5 - P_6$  where the minimum ball and minimum circumscribed ellipsoid enclosing method is applied.

The MOI method utilises a 2D subspace, as in the example in section 4.2, where the load path is represented by a series of points, forming an imaginary homogeneous wire. The method assumes that the mean component of the load path is located at the centre of gravity of the imaginary homogeneous wire (the load path). It is assumed that the deviatoric stress or strain range,  $\Delta S$  and thereby the effective Von Mises stress range,  $\Delta\sigma_{Mises}$ , are depending on the mass moment of inertia. The mass moment of inertia is obtained about the centre of gravity, where the mass

is assumed to be unity. By using this method, the load segments most distant from the centre of gravity will contribute more to the mass moment of inertia and thereby the effective ranges. [Meggiolaro and de Castro, 2011a]

In Meggiolaro and de Castro [2011a] various enclosing surface methods and the MOI method are evaluated in order to predict the fatigue life from an experiment. The fatigue model was not changed and thereby only the method used to determine the effective stress ranges was varied. The results showed good correlation between predicted fatigue life and the experimental fatigue life for the proportional load cases. However, the minimum ball method generally underestimates the effective stress ranges in nonproportional load history, whereas the MOI method takes the nonproportionality into account, by which it predicts the fatigue life within 20 % for all the proposed load cases.

In the FE model, none of these method has been implemented. The stress ranges are determined by the extreme values of the current reversal. However, this may not produce an accurate estimate of the stress ranges. Since the stress ranges are determined from the extreme values, this will produce the greatest stress ranges of the reversal, by which this is conservative, by which a lower fatigue life is estimated.

### 4.3 Multiaxial fatigue

Due to the multiaxial and nonproportional loading of the jacket structure, the assessment of the fatigue life has to be estimated by a proper method. The theory by Stephens et al. [2001] is used in the selection of a fatigue model. The use of equivalent stress or strain method are commonly used, however these methods are only applicable to proportional loading. To handle the nonproportional loading when considering fatigue, it is suggested to use a critical plane model. A critical plane model is derived on the physical basis of a crack. From experiments it was indicated that the nucleation and growth of a crack occurred at specific planes, which is either maximum shear or maximum tensile stress planes [Stephens et al., 2001]. These models relate the fatigue damage to stresses, by which they predict the fatigue life and the orientation of the failure plane.

The critical plane model developed by Findley is based on cyclic shear stress and normal stress. It is applicable for high cycle fatigue, which is above  $10^3$  cycles. The Findley model assumes a linear relation between the allowable alternation shear stress and the maximum normal stress, as seen in equation (4.3), by which the allowable alternating shear stress decreases with increasing maximum normal stress. If no normal stress is applied, then the fatigue constant,  $f$ , and the allowable alternating shear stress are equal. The fatigue constant is a function of the number of cycles to failure, e.g. Basquin's equation, which is used by the S-N approach. The expression for Basquin's equation is seen in equation (4.4) [Stephens et al., 2001, p. 84]. For ductile materials, which is used for the jacket structure, the material constant,  $k$ , is approximately 0.2-0.3 [eFatigue, 2014].

$$\tau_{c\theta} = f - k \sigma_{\theta} \quad (4.3)$$

$$f = A (2 N_f)^B \quad (4.4)$$

where:

[Findley, 1958]

|                  |  |
|------------------|--|
| $f$              | Fatigue constant for given material, [Pa]  |
| $k$              | Material constant which is related to the materials' sensitivity to normal stresses, [-] |
| $\tau_{c\theta}$ | Allowable alternating shear stress at plane angle $\theta$ , [Pa]                        |
| $\sigma_\theta$  | Maximum normal stress at plane angle $\theta$ , [Pa]                                     |
| $A$              | Strength at one cycle (2 reversals), e.g. ultimate tensile strength, [Pa]                |
| $B$              | Slope of S-N curve, [-]  |
| $N_f$            | Number of reversals until failure at given load, [-]                                     |

If the model given in equation (4.3) is used together with equation (4.4), the fatigue life may not be solvable, since there are no restrictions whether the stresses are compressive or tensile. Afterwards, Findley introduces a more complete model, which is able to handle tensile, compressive, and mean stresses. The inputs of the fatigue model are the maximum and alternating stresses, which is shown in equation (4.5).

$$f = \sqrt{\left(\frac{\sigma_A}{2}\right)^2 + \tau_A^2 + k^2 \left(\left(\frac{\sigma_{Max}}{2}\right)^2 + \tau_{Max}^2\right)} + k \frac{\sigma_{Max}}{2} \quad (4.5)$$

where:

[Findley, 1958]

|                |                               |
|----------------|-------------------------------|
| $\sigma_A$     | Normal stress amplitude, [Pa] |
| $\tau_A$       | Shear stress amplitude, [Pa]  |
| $\sigma_{Max}$ | Maximum normal stress, [Pa]   |
| $\tau_{Max}$   | Maximum shear stress, [Pa]    |

The orientation of the failure plane is given in equation (4.6). It is derives from equation (4.3), by introducing the normal and shear stresses as a function of the angle  $\theta$ . Afterwards, the expression is differentiated w.r.t.  $\theta$  in order to determine the critical angle for which the allowable alternating shear stress and the maximum normal stress is in equilibrium.

$$\tan(2\theta) = \frac{\sqrt{\left(\frac{\sigma_A}{2}\right)^2 + \tau_A^2}}{k \sqrt{\left(\frac{\sigma_{Max}}{2}\right)^2 + \tau_{Max}^2}} \quad (4.6)$$

where:

|          |  |
|----------|--|
| $\theta$ | Angle between first principal stress and the plane of the shear stress, [ $^\circ$ ] |
|----------|--|

The fatigue life may be estimated by combining equation (4.4) and (4.5), using the torsional fatigue strength,  $\tau'_f$ . According to eFatigue [2014],  $\tau_f^* = \sqrt{1+k^2} \tau'_f$ , where  $\sqrt{1+k^2} \approx 1.04$ , by which  $k \approx 0.286$ . By isolating  $N_f$ , the fatigue life of the current load level is estimated.

$$\sqrt{\left(\frac{\sigma_A}{2}\right)^2 + \tau_A^2 + k^2 \left(\left(\frac{\sigma_{Max}}{2}\right)^2 + \tau_{Max}^2\right)} + k \frac{\sigma_{Max}}{2} = \tau_f^* (2 N_f)^b \quad (4.7)$$

where:

|            |   |
|------------|---|
| $\tau_f^*$ | Corrected torsional fatigue strength, [-] |
| $b$        | Shear fatigue strength exponent, [-]      |

One of the advantages, even though it is a simple model, is the ability to isolate the number of reversals,  $N_f$ , which is necessary in order to determine the damage sensitivity analytically.



Other critical plane models, such as the Fatemi-Socie model, which may be used to predict the low-cycle fatigue life, has to be solved numerically.

However, in order to ease the calculation of the sensitivity of the fatigue damage, it is assumed that the mean stress is zero. By which the maximum stress is equal to the amplitude. In general is the mean stress known to have significant influence on the fatigue life, where a compressive mean stress extends the fatigue life and a tensile mean stress reduces the fatigue life [Stephens et al., 2001, p. 74]. The  $F_x$  load in figure 2.10 has a significant level of tensile mean stress, by which this assumption may be non-conservative with regards to the fatigue life estimations.

## 4.4 Palmgren-Miner linear damage rule

The Palmgren-Miner linear damage rule is used to assess the damage, using only a numeric value. It is assumed that the measure of damage is defined by the ratio of the number of cycles and the number of cycles until failure. The linear damage rule is shown in equation (4.8). If the damage,  $\eta_{block}$ , is greater than or equal to unity, then failure occur. An additional safety factor is often introduced by requiring the Palmgren-Miner sum to be less than unity, which for off-shore structures typically is about 0.5 [Schjødt-Thomsen, 2012]. However, during the analysis of the jacket structure, the Palmgren-Miner sum is required to be equal to or less than unity.

$$\eta_{block} = \sum_{i=1}^{N_{count}} \frac{n_i}{N_{fi}} \quad (4.8)$$

where:

[Stephens et al., 2001, p. 275]

|                |  |
|----------------|--|
| $\eta_{block}$ | Damage of load history block, [-]                    |
| $N_{count}$    | Number segments in the load history, [-]             |
| $n_i$          | Number of reversals for the load, [-]                |
| $N_{fi}$       | Number of reversals until failure at given load, [-] |

According to RWE Innogy [2014], the wind turbine has a life span of approximately 20 years, by which the jacket structure should be designed to last for at least 20 years. Since the load history, which is applied the jacket structure, is from a 600 s simulation, the damage caused by this load history is scaled to match a 20 years load history. By which, either  $\eta_{block}$  or  $n_i$  is multiplied by 1,051,200 ( $6 \cdot 24 \cdot 365 \cdot 20$ ), assuming a 100 % service life.



Part II

# Optimisation



In this chapter the design variables, cost and constraint functions are defined.

The main task is to minimise the total mass of the jacket structure, while it maintains the required strength w.r.t. fatigue. This is done by use of gradient based optimisation, as described in chapter 8. The structural analysis of the jacket structure is done with a FE analysis.

## 5.1 Design variables

The design variables are parameters which are allowed to change, when searching for the minimum cost function that fulfils the constraints, during the optimisation algorithm. The choice of design variables has an influence on the convergence rate, but it is not required that the design variables explicitly defines the cost function. In this case, the total mass of the jacket structure has to be minimised. This can be accomplished by allowing the geometry and material parameters to be modified during the optimisation. The number of design variables affects the computational time, since the search direction is depending on the sensitivity of cost and constraint functions w.r.t. the design variables. The number of design variables is kept to a minimum by only considering the cross-sectional parameters, which are proportional to the mass of each element. The cross-section of each element in the jacket structure is circular and hollow, by which it is defined by a diameter and a wall thickness.

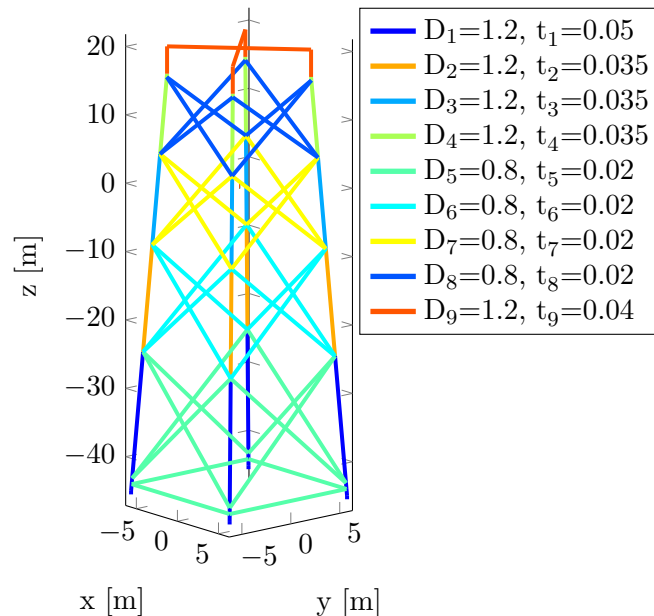


**Figure 5.1** Jacket structure where elements are coloured according to their section properties. The initial parameters, in meters, are shown in the legend box.

The elements within the jacket structure are split into nine section groups to reduce the number of design variables. Each section group is defined by an outer diameter and a wall thickness. The elements within each section group and the initial dimensions are shown in figure 5.1. The

design variable vector is given in equation (5.1). The parameters of section nine are not included, since it is within the concrete block that the wind turbine is attached to:

$$\{x\} = \{D_1, t_1 \dots D_8, t_8\}^T \quad (5.1)$$

## 5.2 Cost function and constraints

The cost function is formulated as a summation of the mass of each element, as shown in equation (5.2). The cross-sectional area is a function of the design variables, by which it has to be recalculated for each design update. The density is assumed to be equal for each element of the jacket structure, by which it may be omitted since it just scales the cost function.

$$f(\{x\}) = \sum_{i=1}^{N_e} \rho L_{ei} A_e(\{x\})_i \quad (5.2)$$

where:

|              |   |
|--------------|---|
| $f(\{x\})$   | Cost function as a function of design variables, [-]                              |
| $\{x\}$      | Design variable vector, [-]   |
| $N_e$        | Number of elements, [-]   |
| $\rho$       | Density, $\left[\frac{\text{kg}}{\text{m}^3}\right]$                              |
| $L_e$        | Length of the element, [m]  |
| $A_e(\{x\})$ | Cross-sectional area of element as a function of design variables, $[\text{m}^2]$ |

The constraint functions are damage criterion based on the Palmgren-Miner sum, where the finite fatigue life of equation (4.7) is inserted. The expression for the constraint function is seen in equation (5.3). The Palmgren-Miner damage is summed for each load segment,  $N_{segments}$ , e.g. for each reversal in the load history. By evaluation of this summation for each reversal,  $n_i$  is unity, by which it is constant and not a function of the rainflow counted reversals. The constraint function is implicitly a function of the design variables, that being the shear and normal stress amplitude, which is a function of the displacements and the design variables. It is a very nonlinear function due to the inverse of an exponential function. This may produce some numerical difficulties when evaluating the damage sensitivity, since a small change in the design variables may result in large changes of the constraint function.

$$g_j(\{x\}) = \sum_{i=1}^{N_{segments}} \frac{n_i}{\exp\left(\frac{\ln\left(\frac{1}{2} \frac{k \sigma_A + \sqrt{k \sigma_A^2 + 4 k \tau_A^2 + \sigma_A^2 + \tau_A^2}}{\tau_f^*}\right)}{b}\right)} - 1 \leq 0 \quad (5.3)$$

for  $j = 1 : N_{samples}$ , where  $N_{samples}$  is the total number of samples in the model, e.g. if the cross-section is evaluated at 4 orientations in each node of the element, each element have 8 samples, by which jacket structure with 108 elements have 864 sample points. However, the number of constraint can greatly be reduced by introduction of an aggregation function. An aggregation function combines all constraints into one effective constraint. One aggregation

function is the p-norm method, shown in equation (5.4), where the  $p$  can be adjusted in order to let the most violated constraint have greater influence in the effective constraint.

$$g(\{x\}) = \left( \sum_{j=1}^{N_{samples}} \left( w_j (g_j - g^0) \right)^p \right)^{\frac{1}{p}} \quad (5.4)$$

where:

[Lund, 2013]

|       |  |
|-------|--|
| $w_j$ | Weight factor, [-]                                 |
| $g^0$ | Ideal value, [-]                                   |
| $p$   | Coefficient to scale most violated constraint, [-] |

### Optimisation problem

Based on the cost and constraint function, described above, the design optimisation problem is defined as:

$$\begin{aligned} \text{Minimise:} & \quad f(\{x\}) \\ \text{Subject to:} & \quad g_j(\{x\}) \leq 0, \quad j = 1 : N_{samples} \end{aligned}$$

By which the total mass of the structure is minimised w.r.t. the fatigue constraints.





# Design Sensitivity Analysis 6

---

This chapter describes the design sensitivity analysis (DSA). DSA is used in the optimisation algorithm to determine the sensitivity of the current design configuration of the cost and constraints. The design sensitivity is the gradient of the function for which sensitivity needs to be determined. The gradient can be determined in different ways, e.g. approximated by a finite difference approximation, analytical by the direct differentiation method, or semi-analytical which is a combination of the former.

The cost function in section 5.2 is directly depending on the design variables, whereas the constraint functions are indirectly depending on the design variables. The constraint functions are depending on the rainflow counted load cycles and the corresponding stresses. The stresses are depending on the displacements from the structural analysis. The structural analysis of the jacket structure is performed using a FE model, which has the following general form (equation (2.1) reprinted):

$$[K] \{D\} = \{R\} \quad (6.1)$$

where:

|         |                                 |
|---------|---------------------------------|
| $[K]$   | Global stiffness matrix, [-]    |
| $\{D\}$ | Global displacement vector, [-] |
| $\{R\}$ | Global load vector, [-]         |

The displacement vector,  $\{D\}$ , depends on the stiffness matrix,  $[K]$ , and load vector,  $\{R\}$ . However, the load vector is not a function of the design variables, whereas the stiffness matrix is. The total derivative of the displacements w.r.t. design variables,  $\frac{d\{D\}}{d\{x\}}$ , is proportional to the total derivative of the stresses, which is used for the determination of the sensitivity of the constraint function.

In the next sections the finite difference method and direct differentiation method are described. The derivations of the cost and constraint sensitivities are described in appendix B.

## 6.1 Finite difference method

The finite difference method is derived from Taylor series expansions. It is used to approximate function values in a segment of the function. The forward difference approximation is first order accurate, by which it halve the number of function evaluations needed. Whereas the central difference approximation is second order accurate. The central difference approximation is applied to a general response function,  $f$ , which is a function of the displacements and the design variables, as seen in equation (6.2). A small perturbation,  $\Delta x_i$ , of the design variable is used in order to approximate the total derivative of the response function. The numeric size of the perturbation should be small compared to the value of the design variable.

$$\frac{df(\{D\}, \{x\})}{dx_i} \approx \frac{f(\{D\}(\{x\} + \Delta x_i), \{x\} + \Delta x_i) - f(\{D\}(\{x\} - \Delta x_i), \{x\} - \Delta x_i)}{2 \Delta x_i} \quad (6.2)$$

where:

[Lund, 2013]

|              |  |
|--------------|--|
| $f$          | General response function, [-]                           |
| $x_i$        | $i^{\text{th}}$ design variable in $\{x\}$ , [-]         |
| $\Delta x_i$ | Perturbation of the $i^{\text{th}}$ design variable, [-] |

The finite difference method can be applied to any function which is at least implicit depending on the state variables, which in this case is the displacements. For instance, if the response function is the stress at a sample point in a element in the FE model, then the response function is implicitly depending on the displacements and the design variables, if they are cross-sectional parameters. Or if the response function is not differentiable using analytical methods, this method will provide the approximated gradient of the response function. Although, for computational expensive function evaluations, it may be more appropriate to determine the gradient of the function analytically if possible.

## 6.2 Direct differentiation method

The direct differentiation method is an analytical method, which is derived using the chain rule. The chain rule can be applied to any multi variable function in order to determine the total derivative of the function. By applying the chain rule to the general form of the FE formulation, in equation (6.1), the expression in equation (6.3) is achieved. The right-hand side of the expression is denoted the pseudo load vector, where the derivatives can be determined analytically since the load vector,  $\{R\}$ , and the stiffness matrix,  $[K]$ , are known. However, if the derivatives are determined using a finite difference approximation, e.g. the central difference method, then this method is denoted semi-analytical. The loads which are applied the jacket structure are independent of the design variables, by which the first term on the right-hand side is zero. It should be noted that the displacements are treated in the global coordinates by which the total derivative of the displacements w.r.t. the design variable also are determined in the global coordinate system. Afterwards, the displacement sensitivities related to the element are transformed into the element coordinate system using the transformation matrix in equation (2.11), as described in section B.2.1, by which it can be used in equation (6.4).

$$[K] \frac{d\{D\}}{dx_i} = \frac{\partial \{R\}}{\partial x_i} - \frac{\partial [K]}{\partial x_i} \{D\} \quad (6.3)$$

[Arora, 2012, p. 582]

The sensitivity of the constraint function,  $g_j$ , w.r.t. the design variables is determined using the direct differentiation method. The constraint function is a function of the displacements and the design variables, by which the chain rule is used. The expression for the constraint sensitivity,  $\frac{dg_j}{dx_i}$ , is seen in equation (6.4), where the derivative of the displacements w.r.t. design variable  $x_i$  is given in equation (6.3).

$$\frac{dg_j}{dx_i} = \frac{\partial g_j}{\partial x_i} + \frac{\partial g_j}{\partial \{D_e\}} \left\{ \frac{d\{D\}}{dx_i} \right\}_l \quad (6.4)$$

[Arora, 2012, p. 582]

The derivation and expressions of the sensitivities are described in appendix B. In chapter 7 is a verification of the implemented design sensitivity analysis, which is conducted using a simple cantilever beam, that only consists of two elements.



# Verification of design sensitivity analysis 7

In this chapter the verification of the design sensitivity analysis is described. The sensitivities obtained from a central difference analysis are compared with the sensitivities determined using the direct differentiation method. If the perturbation used in the central differentiation method is sufficiently small, it is expected that the sensitivities obtained from this method will yield the right result.

A simple cantilever beam model, with two elements is used. By using this simple model the sensitivities are easier to compare. The cantilever beam model is shown in figure 7.1. Node 1 is fixed in all DOF's and the loads are applied at node 3. The two elements are defined by two different section ID's, by which element one is related to section ID one and element two is related to section ID two. For each section an outer diameter and a wall thickness is defined, however the cross-sectional parameters for each section are equal. The elements have a length of 1 m and are circular tubes with an outer diameter of 0.1 m with a wall thickness of 5 mm. The density is  $7800 \text{ kg/m}^3$ , Poisson's ratio is 0.3, and Young's modulus is 210 GPa. The cross-section is evaluated at four places, where the position in the cross-section is seen in the right-hand side of figure 7.2 as the blue dots. On the left-hand side of figure 7.2 are the orientations of the local coordinate systems shown, along with the element numbers.

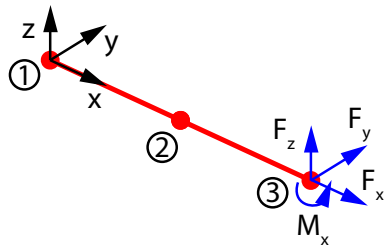


**Figure 7.1** Cantilever beam with two elements, where the circled numbers are the node numbers. Node 1 is fixed in all DOF and the loads are applied at node 3.

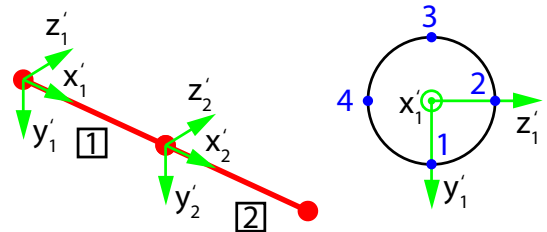


**Figure 7.2** Left: Cantilever beam model, where the local coordinate system is shown. Right: The blue dots are the positions where the cross-section is evaluated for each node in each element.

During the verification of the design sensitivity analysis, the loads are constant, by which the rainfall counting does not influence the sensitivities. The following loads have been applied:  $F_x = 100 \text{ N}$ ,  $F_y = 100 \text{ N}$ ,  $F_z = 100 \text{ N}$ , and  $M_x = 100 \text{ Nm}$ . In figure 7.3 and 7.4 are the normal and shear stress for each sample point shown, respectively. Each sample point is identified by a element number followed by a sample number, e.g. the stress at sample number 14 is named **2,14**:  $xx$ , as this sample point is within element two and  $xx$  is the stress level. The axes of local coordinate systems are the red, green, and blue lines, which are the  $x'$ ,  $y'$ , and  $z'$ -axis, respectively.

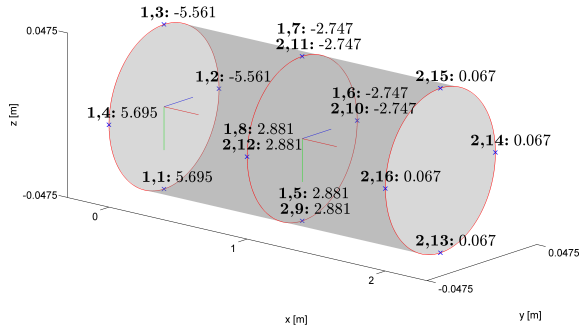


**Figure 7.3** Normal stress in MPa at each sample point, caused by the applied loads.

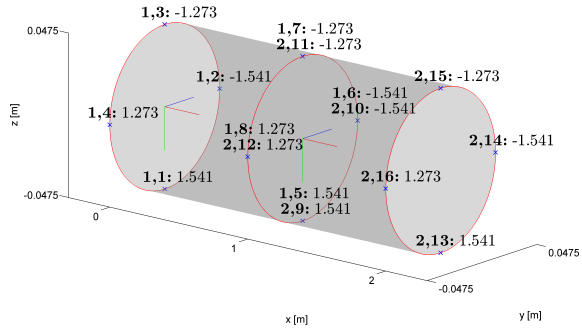


**Figure 7.4** Shear stress in MPa at each sample point, caused by the applied loads.

In the following sections the sensitivities are compared using the central difference method and the direct differentiation method. Only the sensitivities w.r.t. the outer diameter related to section ID one is described in this chapter, however the sensitivities w.r.t. the last three design variables is shown in appendix C. When the central difference method is applied, the design variables have been perturbed by 1/1000 of the initial size of the design variable.

The expressions for the damage sensitivities are depending on stress derivatives. And the expression for the stress sensitivities are depending on displacement derivatives. By which the displacement sensitivity is verified first, followed by stress and damage sensitivities.

## 7.1 Cost sensitivity

The cost sensitivity has been determined using the central difference method and the direct differentiation method. A comparison of the two methods are shown in table 7.1. The mass sensitivity w.r.t. the design variables are determined using direct differentiation method, which yields equation (B.11) and (B.12). By using the central difference method, the mass of the structure is evaluated twice in order to determine the mass sensitivity w.r.t. one of the design variables.

| Method | $\frac{df}{dd_1}$ [kg/m] | $\frac{df}{dt_1}$ [kg/m] | $\frac{df}{dd_2}$ [kg/m] | $\frac{df}{dt_2}$ [kg/m] |
|--------|--------------------------|--------------------------|--------------------------|--------------------------|
| CDM    | 122.5                    | 2202.9                   | 122.5                    | 2202.9                   |
| DDM    | 122.5                    | 2205.4                   | 122.5                    | 2205.4                   |

**Table 7.1** Cost sensitivity determined using the central difference method and the direct differentiation method.

From table 7.1 it is seen that the mass sensitivity w.r.t. the outer diameters are identical. Whereas, the mass sensitivity w.r.t. the wall thickness differ by a small amount, however it was observed that by decreasing the perturbation to 1/10,000 of the design variable, the sensitivity from the central difference method would be identical to the direct differentiation method.

## 7.2 Displacement sensitivity

The displacement sensitivity w.r.t. the outer diameter,  $d_1$ , is shown for each sample point in figure 7.5 and 7.6. The expressions used to determine the displacement sensitivity using the direct differentiation method is described in section B.2.1. The displacement sensitivities determined by the central difference method, are obtained by solving the FE model w.r.t. displacements using the perturbed design variable.

Because the cantilever beam is fixed at  $x = 0$ , there is no change in the displacements at  $x = 0$ , by which the sensitivities are also zero, as seen in figure 7.5 and 7.6. The small values at **1,7** and **2,13** in figure 7.6, which is zero using the central difference method, are caused by numerical inaccuracies. However there is good correlation between the two methods throughout the sample points of the model.

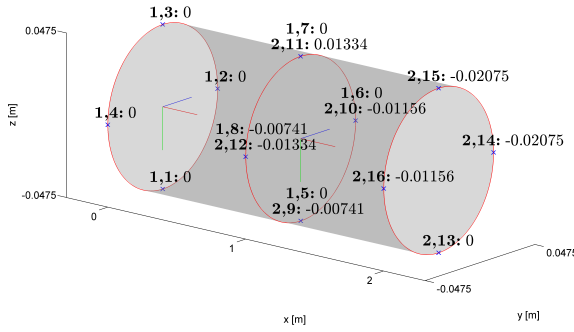


**Figure 7.5** Sensitivity of displacements w.r.t. outer diameter,  $d_1$ , determined using the central difference method, in meters.

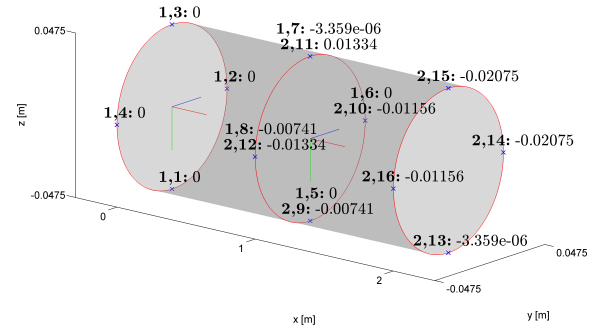


**Figure 7.6** Sensitivity of displacements w.r.t. outer diameter,  $d_1$ , determined using the direct differentiation method, in meters.

## 7.3 Stress sensitivity

In this section the normal and shear stress sensitivities w.r.t. design variable,  $d_1$ , are verified. The derivations for the direct differentiation method are described in section B.2.2 and B.2.3. The FE model is evaluated using the perturbed design variable where the resulting stresses of the FE model are used in order to determine stress sensitivity w.r.t. the design variables, using the central difference method.

### Normal stress sensitivity

The total derivative of the normal stress sensitivity w.r.t. the design variable is given in equation (B.42). From this expression it is seen that the total derivative of the normal stress sensitivity is a function of the displacement sensitivity, which has been verified in section 7.2. By comparing the normal stress sensitivity w.r.t.  $d_1$ , shown in figure 7.7 and 7.8, it shows no difference between the central difference method and the direct differentiation method. However, by including more digits the difference between the two methods is in the region of 500 Pa, by which the difference is negligible.

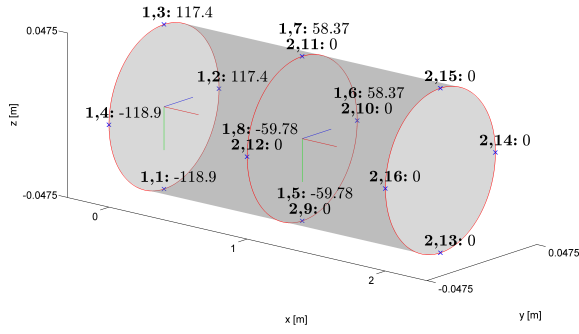


**Figure 7.7** Sensitivity of normal stress w.r.t. outer diameter,  $d_1$ , determined using the central difference method, in MPa/m.

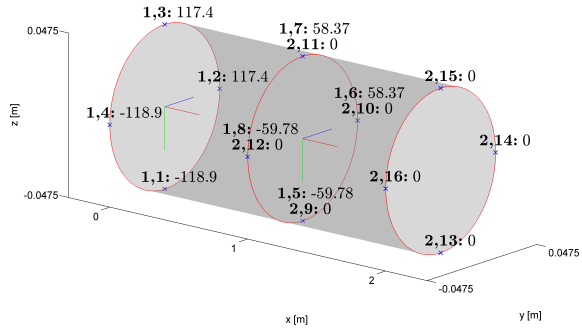


**Figure 7.8** Sensitivity of normal stress w.r.t. outer diameter,  $d_1$ , determined using the direct differentiation method, in MPa/m.

### Shear stress sensitivity

The shear stress sensitivity w.r.t.  $d_1$  is determined using the direct differentiation method, where equation (B.89) is applied, by which the sensitivities are shown in figure 7.10. By using the central difference method, the sensitivities at each sample point are shown in figure 7.9. By comparing the sensitivities determined by the two methods, it shows no differences in the sensitivity. However, like for the normal stress sensitivity, by including more digits the differences are in around 200 Pa.

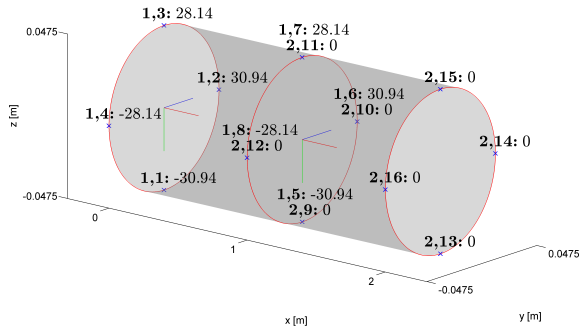


**Figure 7.9** Sensitivity of shear stress w.r.t. outer diameter,  $d_1$ , determined using the central difference method, in MPa/m.

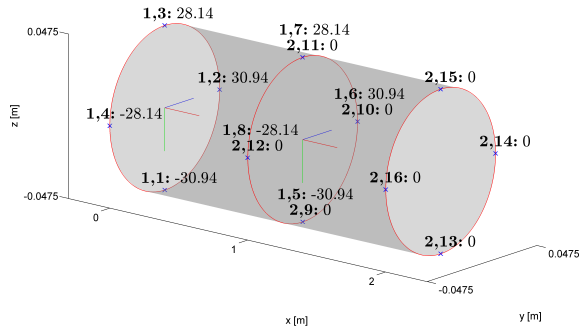


**Figure 7.10** Sensitivity of shear stress w.r.t. outer diameter,  $d_1$ , determined using the direct differentiation method, in MPa/m.

## 7.4 Constraint sensitivity

The damage sensitivity is depending on the partial derivatives of the stresses, however only the total derivatives of the stresses have been verified. The total derivatives of the stresses are functions of the partial derivatives, by which it is assessed that by verifying the total derivatives, the partial derivatives have also been verified. In figure 7.11 is the damage sensitivity w.r.t.  $d_1$  determined using the central difference method and in figure 7.12 is it shown using the direct differentiation method.



In order to evaluate the damage at each sample point, it was necessary to ignore the requirement of the Palmgren-Miner being equal to unity (the rightmost -1 in equation (5.3)), because the calculated damages are very small numbers. When unity is subtracted from this small number, in MATLAB, this would be rounded to -1, by which the damage sensitivity can not be estimated using the central difference method.

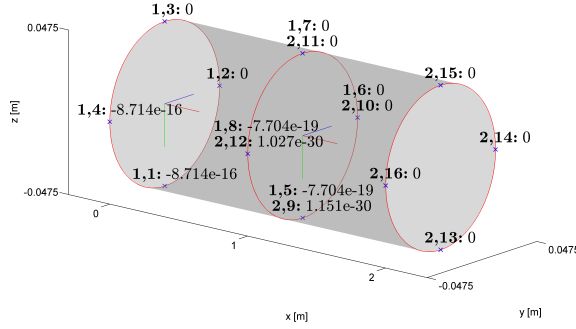


**Figure 7.11** Sensitivity of constraint w.r.t. outer diameter,  $d_1$ , determined using the central difference method.

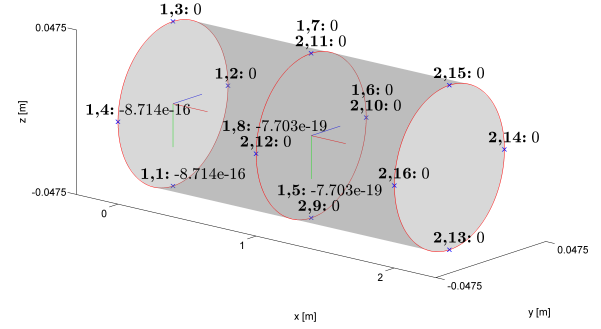


**Figure 7.12** Sensitivity of constraint w.r.t. outer diameter,  $d_1$ , determined using the direct differentiation method.

Generally, there is good correlation between the damage sensitivities, determined using both methods. However, it is difficult to determine whether the values are actual damage sensitivities or if they are caused by numerical inaccuracy, as the numbers are very small.



# Implementation and results

# 8

In this chapter, the choice of optimisation algorithm and the results from using this algorithm is described. The optimisation algorithms available for the `fmincon` solver in MATLAB have been tested, however none of the algorithms were able to find a solution close to the boundary of the constraints. This is because of the very nonlinear constraint function, by which a small change in the design variable, close to the boundary, may have a large impact on the constraints.

The sequential linear programming (SLP) optimisation algorithm has been applied. This algorithm formulates the optimisation as a series of linear sub problems. This is done by introducing move limits to the design variables, by which the optimisation is solved as a linear problem within these move limits. The solution to the linear sub problem is then used as a new design for which new move limits are determined. The size of the move limits is problem dependent.

## Cantilever beam model

The SLP algorithm is examined using the simple cantilever beam model, which is used in the verification of the design sensitivity analysis in chapter 7. The cantilever beam is applied the loads shown in figure 8.1, which are the reduced load history from section 2.5.1, however the magnitude is scaled to fit the cantilever beam model. In order to reduce the computational time, the load history has been reduced further, by which only 1 out of 100 load samples have been included.

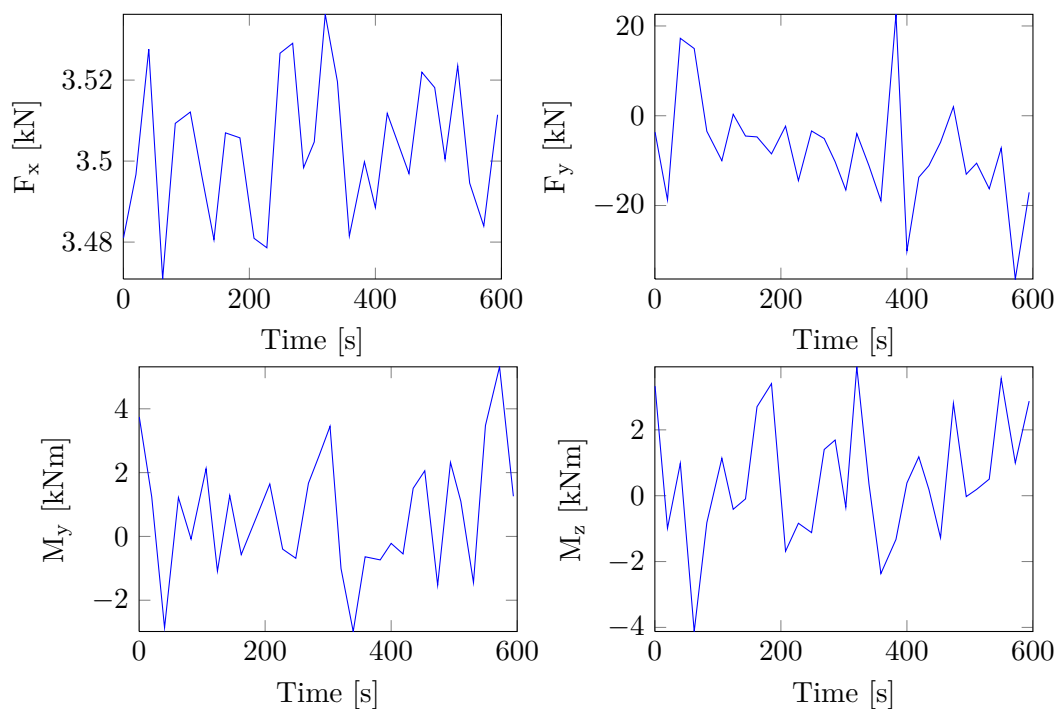


**Figure 8.1** Applied load history at node 3 of the cantilever beam.

The SLP algorithm has been implemented in MATLAB. The framework was handed out as a part of an optimisation course [Lund, 2013], however the code has been modified to suit the optimisation problem in this project. Because of the very nonlinear constraint function, described in section 5.2, the size of the move limits are made changeable during the optimisation. A similar method has been applied by Jørgensen and Nissen [2013]. It should be noted that each design variable has an individual move limit. The move limit criteria is defined by:

- If the change in the constraint gradient is above 5% then the move limit is reduced by 50%
- If the change in the constraint gradient is below 1% then the move limit is increased by 10%

The SLP algorithm is initiated with move limits of 2% of value of the design variables. The results, after 94 iterations, regarding the design variables are shown in table 8.1. It shown an reasonably reduction in the mass of the cantilever beam. However when considering the damage of the optimised structure, seen in figure 8.3, it would be expected that the damage in most of the sample points would be close to the constraint boundary, however only the **1,2** sample point is near the boundary. But comparing to the initial damage distribution, in figure 8.2, there is an increase in the damage of all sample points. Although, an adaptive move limit strategy is applied, the algorithm struggles to achieve an uniform damage distribution throughout the sample points. However by normalising the design variables w.r.t. the constraints it may be possible to achieve an more uniform distribution, since then each design variable would have an equal influence.

|           | Mass [kg] | $d_1$ [m] | $t_1$ [m] | $d_2$ [m] | $t_2$ [m] |
|-----------|-----------|-----------|-----------|-----------|-----------|
| Initial   | 23.28     | 0.1       | 0.005     | 0.1       | 0.005     |
| Optimised | 18.87     | 0.0931    | 0.0044    | 0.0925    | 0.0043    |

**Table 8.1** Mass and design variables before and after optimisation.

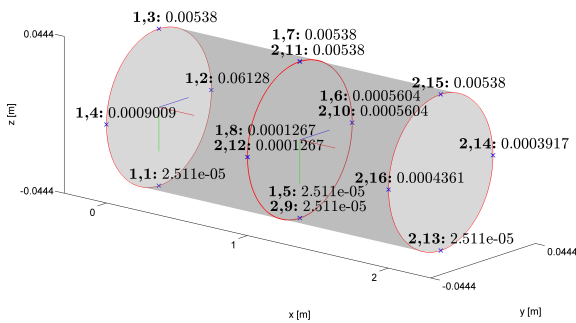


**Figure 8.2** Damage at each sample point, using initial design.

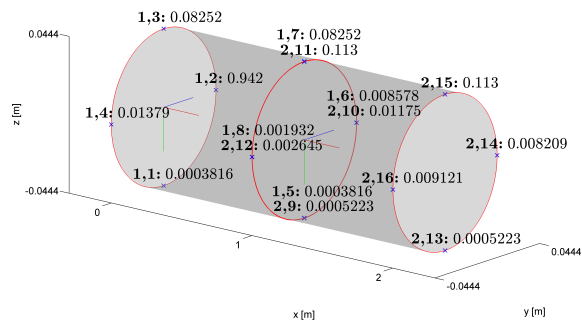


**Figure 8.3** Damage at each sample point, using optimised design.

## Part III

# Evaluation



This project has examined the subject of how to perform a design optimisation, with fatigue as constraint.

A FE model, written in MATLAB, has been developed. The FE model is used in the structural analysis of the jacket structure. The jacket structure is modelled with 3D beam elements, which are based on the Bernoulli-Euler beam theory. The stresses of the elements are evaluated at a finite number of points within the cross-section of each node. The FE code is verified through a simple structure with two elements, by which the displacements, stresses and natural frequencies of the model are compared with an equivalent model in ANSYS. The verification of the FE code showed good agreement with the results from the ANSYS model.

The loads, which are applied to the jacket structure, are nonproportional. The reversals are counted using the modified Wang-Brown rainflow counting method. It is capable of handling nonproportional loading history, whereas the traditional rainflow counting method is not. However, the MWB counting method has not been verified against other methods. The fatigue damage, caused by the loading history, is estimated using the Palmgren-Miner linear damage rule, where the Findley fatigue model is used to estimate the number of reversals before failure at a given stress level.

A design sensitivity analysis has been performed in order to determine the sensitivity of the cost and constraint functions w.r.t. the design variables. The direct difference method is used to determine the sensitivities analytically, where the displacement, stress and damage sensitivities w.r.t. the design variables have been derived and implemented in the FE code. The sensitivities using the direct differentiation method have been verified through a comparison with sensitivities determined by use of the numerical central difference method. The verification has been conducted using a simple cantilever beam model, where the sensitivities at each sample point was determined. The verification of the sensitivities by use of the direct differentiation method showed good agreement with the sensitivities by use of the central difference method.

The framework for a gradient based optimisation has been conducted. The goal for the optimisation is to minimise the total mass of the structure while the damage of each sample point in the structure has to be less than unity. The optimisation is performed using the sequential linear programming algorithm, where adaptive move limits have been implemented. The optimisation is performed for a simple cantilever beam, which showed that the algorithm was able to minimise the mass, however only one sample point was close to the constraint boundary. This has not been investigated further.





In order to perform the optimisation of the jacket structure, the FE code has to be more computationally efficient. As of now, only the global displacements are solved w.r.t. six unity load cases, where the global displacements w.r.t. each load case is used to assemble the global displacement vector caused by the applied loads. This can be done because it is linear model. However, the stresses are proportional to the displacements as well, by which the resulting stresses could also be determined from a linear combination of the pre-calculated stresses due to the unity loads. Since the stresses can be determined from a combination of unity load cases, then the stress sensitivities can be determined in a similar manner. The constraint function is depending on the counted stress ranges by the MWB counting method, by which it cannot be constructed from a combination of unity load cases.

The MWB counting method has not been compared with other methods, by which the performance of this counting method is not known. When dealing with large load histories, the initialisation procedure for the MWB method is quite computationally expensive, due to the reordering of the load history.

The accuracy of the Findley fatigue model has to be considered. However, it is very time consuming to perform fatigue tests, in order to determine the parameters. The Findley model uses a constant,  $k$ , which is related to the materials' sensitivity to normal stress, by which it requires several tests to determine. There are several multiaxial fatigue models available, however the Findley model was chosen because of the simple expression, where the number of reversals until failure can be isolated, which is of great importance in order to determine the sensitivity of the constraint function analytically.

The optimisation was performed using the SLP algorithm, however because of the very nonlinear constraint function, adaptive move limits was used in order to approach the boundary of the constraint function. However a better convergence criteria is needed in order to have a more uniform damage distribution. Likewise by normalising the design variables w.r.t. the constraint function, then a small change of each design variable will contribute an equal amount.



# Bibliography

---

- ANSYS, 2011.** ANSYS. *ANSYS 14.0 Help*, 2011.
- Arora, 2012.** Jasbir S. Arora. *Introduciton to Optimum Design*, 3<sup>rd</sup> edition, 2012.
- Cook, et al., 2001.** Robert D. Cook, David S. Malkus, Michael E. Plesha, and Robert J. Witt. *Concepts and Applications of Finite Element Analysis*, 2001. ISBN: 968-0-471-35605-9.
- eFatigue, 2014.** eFatigue. *Multiaxial Stress-Life Technical Background*, 2014.  
<https://www.efatigue.com/multiaxial/background/stresslife.html>, downloaded: 20-04-2014.
- Energy, N/A.** DTU Wind Energy. *Horizontal Axis Wind turbine simulation Code 2nd generation*, N/A. [www.hawc2.dk](http://www.hawc2.dk).
- Findley, 1958.** W. N. Findley. *A theory for the effect of mean stress on fatigue of metals under combined torsion and axial load or bending*. Division of Engineering, Brown University, 1958.
- Gere and Goodno, 2009.** James M. Gere and Barry J. Goodno. *Mechanics of Materials*, 7 edition, 2009.
- Jonkman, et al., 2 2009.** J. Jonkman, S. Butterfield, W. Musial, and G. Scott. *Definition of a 5-MW Reference Wind Turbine for Offshore System Development*. National Renewable Energy Laboratory, 2 2009. NREL/TP-500-38060.
- Jørgensen and Nissen, 2013.** Jeppe Bjørn Jørgensen and Christian Fløe Nissen. *Analysis and Design Optimization of Offshore Wind Turbine Support Structures*. Master Thesis, Aalborg University, 2013.
- LORC, 2011.** LORC. *Support Structure Concepts For Offshore Wind Turbines*. Lindoe Offshore Renewables Center, 2011. [www.lorc.dk/offshore-wind/foundations](http://www.lorc.dk/offshore-wind/foundations), downloaded: 01-04-2014.
- Lund, 2013.** Eric Lund. *Course on Optimisation theory/Engineering Optimisation*, 2013.  
Slides for lecture 13 - Finite element based analysis and design sensitivity analysis.
- Lund and Overgaard, 2014.** Erik Lund and Lars Chr. T Overgaard. *Fatigue Analysis and Design Optimisation of Offshore Wind Turbine Support Structures*, 2014. Project proposal.
- Meggiolaro and Castro, 2011a.** Marco Antonio Meggiolaro and Jaime Tupiassú Pinho de Castro. *An improved multiaxial rainflow algorithm for non-proportional stress or strain histories – Part I: Enclosing surface methods*. Department of Mechanical Engineering, Pontifical Catholic University of Rio de Janeiro, 2011.
- Meggiolaro and Castro, 2011b.** Marco Antonio Meggiolaro and Jaime Tupiassú Pinho de Castro. *An improved multiaxial rainflow algorithm for non-proportional stress or strain histories – Part II: The Modified Wang–Brown method*. Department of Mechanical Engineering, Pontifical Catholic University of Rio de Janeiro, 2011.

- Offshorewind.biz, 12 2012.** Offshorewind.biz. *STX France Awarded DNV Certification for AG4 Innovative Jacket*, 12 2012. <http://www.offshorewind.biz/2012/12/11/stx-france-awarded-dnv-certification-for-ag4-innovative-jacket>, frontpage image downloaded: 20-5-2014.
- Przemieniecki, 2012.** J. S. Przemieniecki. *Theory of Matrix Structural Analysis*. Dover, 2012. Reprint, originally from 1968, ISBN: 978-0-486-64948-1.
- RWE Innogy, 2014.** RWE Innogy. *FAQs: Offshore Wind Farms*, 2014. <https://www.rwe.com/web/cms/en/1117016/rwe-innogy/about-rwe-innogy/rwe-innogy-uk/useful-information/faqs/offshore-wind-faqs/>, downloaded: 27-05-2014.
- Schjødt-Thomsen, 2012.** Jan Schjødt-Thomsen. *Course on Fracture Mechanics and Fatigue*, 2012. Slides for lecture 12.
- Stephens, et al., 2001.** Ralph I. Stephens, Ali Fatemi, Robert R. Stephens, and Henry O. Fuchs. *Metal Fatigue in Engineering*. Wiley-Interscience, 2 edition, 2001. ISBN: 978-0-471-51059-8.
- Stærdahl, 2008.** Jesper W. Stærdahl. *Course on Finite Element Method II - Structural elements: 3D beam element*. Department of Civil Engineering, 2008. Lecture 6+7, [www.wind.civil.aau.dk/lecture/7sem\\_finite\\_element/Finite\\_element.htm](http://www.wind.civil.aau.dk/lecture/7sem_finite_element/Finite_element.htm), downloaded: 20-02-2014.
- UpWind, 2011.** UpWind. *Work Package 4: Foundations and Support Structures*, 2011. [www.upwind.eu](http://www.upwind.eu).
- Vorpahl, Popko, and Kaufer, 2011.** Fabian Vorpahl, Wojciech Popko, and Daniel Kaufer. *Description of a basic model of the "UpWind reference jacket" for code comparison in the OC4 project under IEA Wind Annex XXX*. Institute for Wind Energy and Energy System Technology, 2011.
- Wang and Brown, 1996.** C. H. Wang and M. W. Brown. *Life Prediction Techniques for Variable Amplitude Multiaxial Fatigue - Part 1: Theories*. Journal of Engineering Materials and Technology, 1996. Vol. 118(3), pp. 367-370.

Part IV

# Appendix



## A

The element technology, which is used in the ANSYS model, is called 'BEAM188'. It is a two node 3D beam element and is based on the Timoshenko beam theory, whereas in the MATLAB code Bernoulli-Euler beam theory is used. The difference between Bernoulli-Euler and Timoshenko beam theory is that the cross-section is allowed to rotate by assuming that the transverse shear strain is constant through the cross-section. The non-default element settings are shown in table A.1.

| Key option | Value of key option | Description  |
|------------|---------------------|--|
| KEYOPT(3)  | 3                   | Cubic shape functions along the length   |
| KEYOPT(4)  | 2                   | Output combined torsion- and flexure-related transverse shear stress                   |
| KEYOPT(6)  | 3                   | Output section forces/moments and strains/curvatures extrapolated to the element nodes |

**Table A.1** BEAM188 element key options, which are not default. [ANSYS, 2011]

A MATLAB script has been written, which translates the FE model in MATLAB to be used in ANSYS Classic. That being, nodal positions, element connections, section properties, static loads and boundary conditions, by which the main ANSYS script only consists of the essential parts in order to solve the system and post processing commands. In figure A.1 is the discretised cross-section used in ANSYS. The minimum cross-sectional elements in ANSYS is 8. During the verification of the FE code, the mean value of the outer and inner stresses are used, e.g. the stress at the intersection of element 3 and 5 is the mean stress of node 7 and 8.

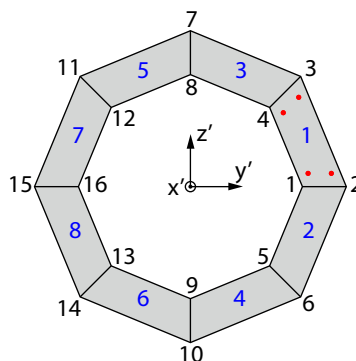


**Figure A.1** Section plot, where the blue and black numbers are element and node numbers, respectively. The red dots illustrates the placement of the integration points within each element.

The ten lowest natural frequencies have been solved using a modal analysis, where the Block Lanczos method is applied.





# DSA derivations

# B

This appendix describes the derivations of the sensitivities determined using the direct differentiation method. Furthermore, this supports the description of the design sensitivity analysis in chapter 6 and a verification of these expressions, implemented in the FE model, are conducted in chapter 7. In the following derivations, the function dependencies are not denoted in the expression, in order to make the expressions easier to read. The sensitivities are determined w.r.t. to the design variables,  $\{x\} = [d \ t]^T$ .

During the derivations, the following expressions for the cross-sectional area, the moment of inertia, polar moment of inertia, and the local y' and z' distances to the point of evaluation. Furthermore, expressions described in chapter 2 are used, e.g. the expressions for the local stiffness matrix.

$$A_e = \pi (d t - t^2) \quad (\text{B.1})$$

$$I_y = \pi \frac{d^4 - (d - 2t)^4}{64} \quad (\text{B.2})$$

$$I_z = \pi \frac{d^4 - (d - 2t)^4}{64} \quad (\text{B.3})$$

$$J_x = \pi \frac{d^4 - (d - 2t)^4}{32} \quad (\text{B.4})$$

$$Y = \frac{d - t}{2} \cos(\beta) \quad (\text{B.5})$$

$$Z = -\frac{d - t}{2} \sin(\beta) \quad (\text{B.6})$$

## B.1 Cost function sensitivity

The cost function of the system, is the combined mass of the structure. The cost function as a function of the current design is shown in equation (5.2). In order to determine the mass sensitivity w.r.t. the design variables, the direct differentiation method are applied. The only term, which is depending on the design variables is the cross-sectional area of the element by which the sensitivity is determined by equation (B.7). The sensitivity contributions is summed for all elements which is associated with the current design variable.

$$\frac{df}{dx_i} = \sum_{ei=1}^{N_{ei}} \frac{df}{dA_e} \frac{\partial A_e}{\partial x_i} \quad (\text{B.7})$$

where:

|          |  |
|----------|--|
| $f$      | Cost function as a function of design variables, [kg]                  |
| $x_i$    | $i^{\text{th}}$ design variable in $\{x\}$ , [-]                       |
| $N_{ei}$ | Number of elements associated the $i^{\text{th}}$ design variable, [-] |

Where the total derivative of the cost function w.r.t. the cross-sectional area of the element is

given as:

$$\frac{df}{dA_e} = \rho L_e \quad (\text{B.8})$$

The partial derivatives of the cross-sectional area of the element w.r.t. the design variables are determined in equation (B.9) and (B.10).

$$\frac{\partial A_e}{\partial d} = \pi t \quad (\text{B.9})$$

$$\frac{\partial A_e}{\partial t} = \pi (d - 2t) \quad (\text{B.10})$$

By inserting equation (B.8) and (B.9) into equation (B.8), the mass sensitivity w.r.t. design variable  $d$  is given in equation (B.11). Likewise, the mass sensitivity w.r.t. design variable  $t$  is obtained by inserting equation (B.8) and (B.10) into equation (B.8), which is shown in equation (B.12).

$$\frac{df}{dd} = \sum_{i=1}^{N_{ei}} \rho L_e \pi t \quad (\text{B.11})$$

$$\frac{df}{dt} = \sum_{i=1}^{N_{ei}} \rho L_e \pi (d - 2t) \quad (\text{B.12})$$

The gradient vector of the cost function is assembled as shown in equation (B.13). If the gradient of the cost function is evaluated w.r.t. more design variables, then more rows are added to equation (B.13).

$$\{c\} = \begin{Bmatrix} \frac{df}{dd} \\ \frac{df}{dt} \end{Bmatrix} \quad (\text{B.13})$$

where:

$$\{c\} \mid \text{Gradient of cost function w.r.t. design variables, [-]}$$

## B.2 Constraint function sensitivity

The constraint function measures the damage of the sample point caused by the applied load. The expression of the constraint function is shown in equation (5.3). The sensitivity of the constraint function w.r.t. the design variables is determined by equation (B.14). The local displacement vector is seen in equation (2.2).

$$\frac{dg_j}{dx_i} = \frac{\partial g_j}{\partial x_i} + \frac{\partial g_j^T}{\partial \{D_e\}} \left\{ \frac{d\{D\}}{dx_i} \right\}_l \quad (\text{B.14})$$

where:

$$\{D_e\} \mid \text{Local element displacement vector, [-]}$$

The expressions for the partial derivatives of the constraint function w.r.t. the design variables and the displacements are shown in equation (B.15) and (B.16).

$$\frac{\partial g_j}{\partial x_i} = \frac{dg_j}{d\sigma_A} \frac{\partial \sigma_A}{\partial x_i} + \frac{dg_j}{d\tau_A} \frac{\partial \tau_A}{\partial x_i} \quad (\text{B.15})$$

$$\frac{\partial g_j^T}{\partial \{D_e\}} = \frac{dg_j}{d\sigma_A} \frac{\partial \sigma_A}{\partial \{D_e\}} + \frac{dg_j}{d\tau_A} \frac{\partial \tau_A}{\partial \{D_e\}} \quad (\text{B.16})$$

The total derivatives of the constraint function w.r.t. normal and shear stress are shown in equation (B.17) and (B.18). The partial derivative of the normal stress w.r.t. the design variables and displacements are shown in equation (B.74), (B.75), and (B.87). The total derivative of the displacement w.r.t. the design variables is described in section B.2.1.

$$\frac{dg_j}{d\sigma_A} = - \frac{n_i \left( 2k \sqrt{(\sigma_A^2 + 4\tau_A^2)(4k+1)} + 4k\sigma_A + \sigma_A \right) \exp \left( \frac{2 \ln(2) - \ln \left( \frac{2k\sigma_A + \sqrt{(\sigma_A^2 + 4\tau_A^2)(4k+1)}}{\tau_f^*} \right)}{b} \right)}{\sqrt{(\sigma_A^2 + 4\tau_A^2)(4k+1)} \left( 2k\sigma_A + \sqrt{(\sigma_A^2 + 4\tau_A^2)(4k+1)} \right) b} \quad (\text{B.17})$$

$$\frac{dg_j}{d\tau_A} = - \frac{n_i 4\tau_A (4k+1) \exp \left( \frac{2 \ln(2) - \ln \left( \frac{2k\sigma_A + \sqrt{(\sigma_A^2 + 4\tau_A^2)(4k+1)}}{\tau_f^*} \right)}{b} \right)}{\sqrt{(\sigma_A^2 + 4\tau_A^2)(4k+1)} \left( 2k\sigma_A + \sqrt{(\sigma_A^2 + 4\tau_A^2)(4k+1)} \right) b} \quad (\text{B.18})$$

The damage sensitivity w.r.t. design variables, in equation (B.14) are determined for each sample point. The partial derivative of the damage sensitivity w.r.t. the displacements are w.r.t. the global coordinate system, by which the total derivative of the displacements w.r.t. the design variables are also w.r.t. the global coordinate system.

Since the damage sensitivity depend on configuration of the FE modelled structure, a single expression, which combines equation (B.14) to (B.18) cannot be determined. Therefore, the expression for damage sensitivity at a sample point has to be assembled from the partial and total derivatives which is related to the current sample point.

The gradient of the constraint function is assembled in a matrix, where the  $i$  index denotes the row and the  $j$  index denotes the column. The indices are according to equation (B.14).

### B.2.1 Displacement sensitivity

In this subsection the derivation of the displacement sensitivity w.r.t. the design variable are described. The direct differentiation method is applied to the general FE formulation, by which the following expression is determined (equation (6.3) reprinted):

$$[K] \frac{d\{D\}}{dx_i} = \frac{\partial \{R\}}{\partial x_i} - \frac{\partial [K]}{\partial x_i} \{D\} \quad (\text{B.19})$$

where:

|         |                                 |
|---------|---------------------------------|
| $[K]$   | Global stiffness matrix, [-]    |
| $\{D\}$ | Global displacement vector, [-] |
| $\{R\}$ | Global load vector, [-]         |

The displacement sensitivity, on the left-hand side of equation (B.19), is determined in the global coordinate system. Since, the stress and damage sensitivities are expressed w.r.t. the element coordinate system, the displacement sensitivities related to the element are transformed using the transformation matrix in equation (2.11). This is shown in equation (B.20), where  $\left\{ \frac{d\{D\}}{dx_i} \right\}_g$  are the global displacement sensitivities related to the element.

$$\left\{ \frac{d\{D\}}{dx_i} \right\}_l = [T] \left\{ \frac{d\{D\}}{dx_i} \right\}_g \quad (\text{B.20})$$

where:

$$[T] \mid \text{Transformation matrix, [-]}$$

The partial derivative of the global element stiffness matrix w.r.t.  $d$  are derived by differentiation of the  $X, S, Y_i$ , and  $Z_i$  expressions from equation (2.4) w.r.t. design variable,  $d$ . By which equation (B.21) to (B.30) are derived. The partial derivative of the global element stiffness matrix w.r.t.  $d$  are determined using equation (B.31) to (B.40).

$$\frac{\partial X}{\partial d} = E \frac{\pi t}{L_e} \quad (\text{B.21})$$

$$\frac{\partial S}{\partial d} = G \frac{\pi d^3 - (d - 2t)^3}{8 L_e} \quad (\text{B.22})$$

$$\frac{\partial Y_1}{\partial d} = 12 E \frac{\pi d^3 - (d - 2t)^3}{16 L_e^3} \quad (\text{B.23})$$

$$\frac{\partial Y_2}{\partial d} = 6 E \frac{\pi d^3 - (d - 2t)^3}{16 L_e^2} \quad (\text{B.24})$$

$$\frac{\partial Y_3}{\partial d} = 4 E \frac{\pi d^3 - (d - 2t)^3}{16 L_e} \quad (\text{B.25})$$

$$\frac{\partial Y_4}{\partial d} = 2 E \frac{\pi d^3 - (d - 2t)^3}{16 L_e} \quad (\text{B.26})$$

$$\frac{\partial Z_1}{\partial d} = 12 E \frac{\pi d^3 - (d - 2t)^3}{16 L_e^3} \quad (\text{B.27})$$

$$\frac{\partial Z_2}{\partial d} = 6 E \frac{\pi d^3 - (d - 2t)^3}{16 L_e^2} \quad (\text{B.28})$$

$$\frac{\partial Z_3}{\partial d} = 4 E \frac{\pi d^3 - (d - 2t)^3}{16 L_e} \quad (\text{B.29})$$

$$\frac{\partial Z_4}{\partial d} = 2 E \frac{\pi d^3 - (d - 2t)^3}{16 L_e} \quad (\text{B.30})$$

$$\frac{\partial X}{\partial t} = E \frac{\pi (d - 2t)}{L_e} \quad (\text{B.31})$$

$$\frac{\partial S}{\partial t} = G \frac{\pi (d - 2t)^3}{4 L_e} \quad (\text{B.32})$$

$$\frac{\partial Y_1}{\partial t} = 3 E \frac{\pi (d - 2t)^3}{2 L_e^3} \quad (\text{B.33})$$

$$\frac{\partial Y_2}{\partial t} = 3 E \frac{\pi (d - 2t)^3}{2 L_e^2} \quad (\text{B.34})$$

$$\frac{\partial Y_3}{\partial t} = E \frac{\pi (d - 2t)^3}{2 L_e} \quad (\text{B.35})$$

$$\frac{\partial Y_4}{\partial t} = E \frac{\pi (d - 2t)^3}{4 L_e} \quad (\text{B.36})$$

$$\frac{\partial Z_1}{\partial t} = 3 E \frac{\pi (d - 2t)^3}{2 L_e^3} \quad (\text{B.37})$$

$$\frac{\partial Z_2}{\partial t} = 3 E \frac{\pi (d - 2t)^3}{2 L_e^2} \quad (\text{B.38})$$

$$\frac{\partial Z_3}{\partial t} = E \frac{\pi (d - 2t)^3}{2 L_e} \quad (\text{B.39})$$

$$\frac{\partial Z_4}{\partial t} = E \frac{\pi (d - 2t)^3}{4 L_e} \quad (\text{B.40})$$

### B.2.2 Normal stress sensitivity

The normal stress at a sample point is determined using the following expression:

$$\sigma_A = \frac{N_x}{A_e} - \frac{M_z Y}{I_z} - \frac{M_y Z}{I_y} \quad (\text{B.41})$$

In order to determine the total derivative of the normal stress, the direct differentiation methods is applied, since the normal stress is a function of the displacements and the design variables,

however the displacements are also a function of design variables.

$$\frac{d\sigma_A}{dx_i} = \frac{\partial\sigma_A}{\partial x_i} + \frac{\partial\sigma_A}{\partial\{D_e\}} \left\{ \frac{d\{D\}}{dx_i} \right\}_l \quad (\text{B.42})$$

### Sensitivity w.r.t. design variables

The partial derivative of the normal stress w.r.t. the design variable is shown in equation (B.43), where the chain rule have been applied.

$$\begin{aligned} \frac{\partial\sigma_A}{\partial x_i} = & \frac{d\sigma_A}{dN_x} \frac{\partial N_x}{\partial x_i} + \frac{d\sigma_A}{dA_e} \frac{\partial A_e}{\partial x_i} + \frac{d\sigma_A}{dM_z} \frac{\partial M_z}{\partial x_i} + \frac{d\sigma_A}{dY} \frac{\partial Y}{\partial x_i} + \frac{d\sigma_A}{dI_z} \frac{\partial I_z}{\partial x_i} + \\ & \frac{d\sigma_A}{dM_y} \frac{\partial M_y}{\partial x_i} + \frac{d\sigma_A}{dZ} \frac{\partial Z}{\partial x_i} + \frac{d\sigma_A}{dI_y} \frac{\partial I_y}{\partial x_i} \end{aligned} \quad (\text{B.43})$$

The total derivatives in equation (B.43) are expressed in equation (B.44) to (B.51).

$$\frac{d\sigma_A}{dN_x} = \frac{1}{A_e} \quad (\text{B.44})$$

$$\frac{d\sigma_A}{dM_z} = \frac{-Y}{I_z} \quad (\text{B.45})$$

$$\frac{d\sigma_A}{dY} = \frac{-M_z}{I_z} \quad (\text{B.46})$$

$$\frac{d\sigma_A}{dI_z} = \frac{M_z Y}{I_z^2} \quad (\text{B.47})$$

$$\frac{d\sigma_A}{dA_e} = \frac{-N_x}{A_e^2} \quad (\text{B.48})$$

$$\frac{d\sigma_A}{dM_y} = \frac{-Z}{I_y} \quad (\text{B.49})$$

$$\frac{d\sigma_A}{dZ} = \frac{-M_y}{I_y} \quad (\text{B.50})$$

$$\frac{d\sigma_A}{dI_y} = \frac{M_y Z}{I_y^2} \quad (\text{B.51})$$

The partial derivatives w.r.t. the design variables in equation (B.43) are expressed in equation (B.53) to (B.61). However, since the expressions for  $N_x$ ,  $M_y$ , and  $M_z$  are implicit depending on the design variables, the chain rule has to be applied in order to determine the partial derivatives of  $N_x$ ,  $M_y$ , and  $M_z$ .

$$\frac{\partial A_e}{\partial d} = \pi t \quad (\text{B.52})$$

$$\frac{\partial Y}{\partial d} = \frac{\cos(\beta)}{2} \quad (\text{B.53})$$

$$\frac{\partial I_z}{\partial d} = \pi \frac{d^3 - (d - 2t)^3}{16} \quad (\text{B.54})$$

$$\frac{\partial Z}{\partial d} = \frac{-\sin(\beta)}{2} \quad (\text{B.55})$$

$$\frac{\partial I_y}{\partial d} = \pi \frac{d^3 - (d - 2t)^3}{16} \quad (\text{B.56})$$

$$\frac{\partial A_e}{\partial t} = \pi (d - 2t) \quad (\text{B.57})$$

$$\frac{\partial Y}{\partial t} = \frac{-\cos(\beta)}{2} \quad (\text{B.58})$$

$$\frac{\partial I_z}{\partial t} = \pi \frac{(d - 2t)^3}{8} \quad (\text{B.59})$$

$$\frac{\partial Z}{\partial t} = \frac{\sin(\beta)}{2} \quad (\text{B.60})$$

$$\frac{\partial I_y}{\partial t} = \pi \frac{(d - 2t)^3}{8} \quad (\text{B.61})$$

The partial derivatives of  $N_x$ ,  $M_y$ , and  $M_z$  w.r.t. the design variables are expressed as follows:

$$\frac{\partial N_x}{\partial x_i} = \frac{dN_x}{dA_e} \frac{\partial A_e}{\partial x_i} \quad (\text{B.62})$$

$$\frac{\partial M_y}{\partial x_i} = \frac{dM_y}{dI_y} \frac{\partial I_y}{\partial x_i} \quad (\text{B.63})$$

$$\frac{\partial M_z}{\partial x_i} = \frac{dM_z}{dI_z} \frac{\partial I_z}{\partial x_i} \quad (\text{B.64})$$

The total derivatives in equation (B.62) to (B.64) are expressed in equation (B.65) to (B.67).

$$\frac{dM_y}{dI_y} = E \kappa_y \quad (\text{B.65})$$

$$\frac{dN_x}{dA_e} = \frac{E \Delta u}{L_e} \quad (\text{B.66})$$

$$\frac{dM_z}{dI_z} = E \kappa_z \quad (\text{B.67})$$

The partial derivatives of  $N_x$ ,  $M_y$ , and  $M_z$  w.r.t. the design variables are expressed as follows:

$$\frac{\partial N_x}{\partial d} = \pi t \frac{E \Delta u}{L_e} \quad (\text{B.68})$$

$$\frac{\partial M_z}{\partial d} = E \kappa_z \pi \frac{d^3 - (d - 2t)^3}{16} \quad (\text{B.69})$$

$$\frac{\partial M_y}{\partial d} = E \kappa_y \pi \frac{d^3 - (d - 2t)^3}{16} \quad (\text{B.70})$$

$$\frac{\partial N_x}{\partial t} = \pi (d - 2t) \frac{E \Delta u}{L_e} \quad (\text{B.71})$$

$$\frac{\partial M_z}{\partial t} = E \kappa_z \pi \frac{(d - 2t)^3}{8} \quad (\text{B.72})$$

$$\frac{\partial M_y}{\partial t} = E \kappa_y \pi \frac{(d - 2t)^3}{8} \quad (\text{B.73})$$

By inserting the above expressions into equation (B.43), the partial derivative of the normal stress w.r.t. the design variables are given in equation (B.74) and (B.75). Note that the sensitivity is only depending on the curvature, Young's modulus, and the angle, in the cross-section, of the evaluated sample point.

$$\frac{\partial \sigma_A}{\partial d} = \frac{E \kappa_y \sin(\beta)}{2} - \frac{E \kappa_z \cos(\beta)}{2} \quad (\text{B.74})$$

$$\frac{\partial \sigma_A}{\partial t} = \frac{E \kappa_z \cos(\beta)}{2} - \frac{E \kappa_y \sin(\beta)}{2} \quad (\text{B.75})$$

### Sensitivity w.r.t. displacements

The sensitivity of the normal stress w.r.t. displacements are described below. The normal stress is determined using equation (B.76).

$$\sigma_A = \frac{N_x}{A_e} - \frac{M_z Y}{I_z} - \frac{M_y Z}{I_y} \quad (\text{B.76})$$

Again, the chain rule is applied, due to the multi variable function, by which the partial derivative of the normal stress w.r.t. displacements are determined using equation (B.77).

$$\frac{\partial \sigma_A}{\partial \{D_e\}} = \frac{d\sigma_A}{dN_x} \frac{\partial N_x}{\partial \{D_e\}} + \frac{d\sigma_A}{dM_y} \frac{\partial M_y}{\partial \{D_e\}} + \frac{d\sigma_A}{dM_z} \frac{\partial M_z}{\partial \{D_e\}} \quad (\text{B.77})$$

The total derivatives of  $\sigma_A$  w.r.t.  $N_x$ ,  $M_z$ , and  $M_y$  are given in equation (B.44), (B.45), and (B.49), respectively. The partial derivatives of  $N_x$ ,  $M_y$ , and  $M_z$  w.r.t. displacements are expressed in equation (B.78) to (B.80).

$$\frac{\partial N_x}{\partial \{D_e\}} = \frac{dN_x}{d\Delta u} \frac{\partial \Delta u}{\partial \{D_e\}} \quad (\text{B.78})$$

$$\frac{\partial M_y}{\partial \{D_e\}} = \frac{dM_y}{d\kappa_y} \frac{\partial \kappa_y}{\partial \{D_e\}} \quad (\text{B.79})$$

$$\frac{\partial M_z}{\partial \{D_e\}} = \frac{dM_z}{d\kappa_z} \frac{\partial \kappa_z}{\partial \{D_e\}} \quad (\text{B.80})$$

The total derivatives in equation (B.78) to (B.80) are determined below:

$$\frac{dN_x}{d\Delta u} = \frac{E A_e}{L_e} \quad (\text{B.81})$$

$$\frac{dM_y}{d\kappa_y} = E I_y \quad (\text{B.82})$$

$$\frac{dM_z}{d\kappa_z} = E I_z \quad (\text{B.83})$$

The partial derivatives of  $\Delta u$ ,  $\kappa_y$ , and  $\kappa_z$  w.r.t. the displacements are shown in equation (B.84) to (B.86).

$$\frac{\partial \Delta u}{\partial \{D_e\}} = \left\{ \begin{matrix} -1 & 0 & 0 & 0 & 0 & 0 & 1 & 0 & 0 & 0 & 0 & 0 \end{matrix} \right\}^T \quad (\text{B.84})$$

$$\frac{\partial \kappa_y}{\partial \{D_e\}} = \left\{ \begin{matrix} 0 & 0 & \frac{12x+6}{L_e^2} & 0 & \frac{6x-4}{L_e} & 0 & 0 & 0 & \frac{12x-6}{L_e^2} & 0 & \frac{6x-2}{L_e} & 0 \end{matrix} \right\}^T \quad (\text{B.85})$$

$$\frac{\partial \kappa_z}{\partial \{D_e\}} = \left\{ \begin{matrix} 0 & \frac{12x-6}{L_e^2} & 0 & 0 & 0 & \frac{6x-4}{L_e} & 0 & \frac{12x+6}{L_e^2} & 0 & 0 & 0 & \frac{6x-2}{L_e} \end{matrix} \right\}^T \quad (\text{B.86})$$

By inserting the above expressions into equation (B.77), the partial derivative of the normal stress w.r.t. displacements are given in equation (B.87).

$$\frac{\partial \sigma_A}{\partial \{D_e\}} = \left\{ \begin{matrix} \frac{-E}{L_e} \\ -E \frac{\cos(\beta) (12x-6) (d-t)}{2 L_e^2} \\ -E \frac{\sin(\beta) (12x-6) (d-t)}{2 L_e^2} \\ 0 \\ E \frac{\sin(\beta) (6x-4) (d-t)}{2 L_e} \\ -E \frac{\cos(\beta) (6x-4) (d-t)}{2 L_e} \\ \frac{E}{L_e} \\ E \frac{\cos(\beta) (12x-6) (d-t)}{2 L_e^2} \\ E \frac{\sin(\beta) (12x-6) (d-t)}{2 L_e^2} \\ 0 \\ E \frac{\sin(\beta) (6x-2) (d-t)}{2 L_e} \\ -E \frac{\cos(\beta) (6x-2) (d-t)}{2 L_e} \end{matrix} \right\} \quad (\text{B.87})$$

### B.2.3 Shear stress sensitivity

The total shear stress is determined using the expression in equation (B.88).

$$\tau_A = \frac{V_y Q_y}{I_z 2 b_1} + \frac{V_z Q_z}{I_y 2 b_2} + \frac{T_x Z}{J_x} + \frac{T_x Y}{J_x} \quad (\text{B.88})$$

where  $b_1 = b(\beta)$  and  $b_2 = b(90^\circ - \beta)$ , according to equation (2.32).

In order to determine the total derivative of the shear stress, the direct differentiation methods are applied, since the shear stress is a function of the displacements, which is depending on the design variables, and a function of the design variables.

$$\frac{d\tau_A}{dx_i} = \frac{\partial \tau_A}{\partial x_i} + \frac{\partial \tau_A}{\partial \{D_e\}} \left\{ \frac{d\{D\}}{dx_i} \right\}_l \quad (\text{B.89})$$

#### Sensitivity w.r.t. design variables

The partial derivative of the shear stress w.r.t. the design variable is shown in equation (B.90), where the chain rule have been applied.

$$\begin{aligned} \frac{\partial \tau_A}{\partial x_i} = & \frac{d\tau_A}{dV_y} \frac{\partial V_y}{\partial x_i} + \frac{d\tau_A}{dI_y} \frac{\partial I_y}{\partial x_i} + \frac{d\tau_A}{dQ_y} \frac{\partial Q_y}{\partial x_i} + \frac{d\tau_A}{db_1} \frac{\partial b_1}{\partial x_i} + \\ & \frac{d\tau_A}{dV_z} \frac{\partial V_z}{\partial x_i} + \frac{d\tau_A}{dI_z} \frac{\partial I_z}{\partial x_i} + \frac{d\tau_A}{dQ_z} \frac{\partial Q_z}{\partial x_i} + \frac{d\tau_A}{db_2} \frac{\partial b_2}{\partial x_i} + \\ & \frac{d\tau_A}{dT_x} \frac{\partial T_x}{\partial x_i} + \frac{d\tau_A}{dJ_x} \frac{\partial J_x}{\partial x_i} + \frac{d\tau_A}{dZ} \frac{\partial Z}{\partial x_i} + \frac{d\tau_A}{dY} \frac{\partial Y}{\partial x_i} \end{aligned} \quad (\text{B.90})$$

The total derivatives in equation (B.90) are expressed in equation (B.91) to (B.102).

$$\frac{d\tau_A}{dV_y} = \frac{Q_y}{2 I_z b_1} \quad (\text{B.91})$$

$$\frac{d\tau_A}{dI_y} = -\frac{Q_z V_z}{2 I_y^2 b_2} \quad (\text{B.92})$$

$$\frac{d\tau_A}{dQ_y} = \frac{V_y}{2 I_z b_1} \quad (\text{B.93})$$

$$\frac{d\tau_A}{db_1} = -\frac{Q_y V_y}{2 I_z b_1^2} \quad (\text{B.94})$$

$$\frac{d\tau_A}{dT_x} = \frac{Y + Z}{J_x} \quad (\text{B.95})$$

$$\frac{d\tau_A}{dZ} = \frac{T_x}{J_x} \quad (\text{B.96})$$

$$\frac{d\tau_A}{dV_z} = \frac{Q_z}{2 I_y b_2} \quad (\text{B.97})$$

$$\frac{d\tau_A}{dI_z} = -\frac{Q_y V_y}{2 I_z^2 b_1} \quad (\text{B.98})$$

$$\frac{d\tau_A}{dQ_z} = \frac{V_z}{2 I_y b_2} \quad (\text{B.99})$$

$$\frac{d\tau_A}{db_2} = -\frac{Q_z V_z}{2 I_y b_2^2} \quad (\text{B.100})$$

$$\frac{d\tau_A}{dJ_x} = -T_x \frac{Y + Z}{J_x^2} \quad (\text{B.101})$$

$$\frac{d\tau_A}{dY} = \frac{T_x}{J_x} \quad (\text{B.102})$$

Where the partial derivatives, in equation (B.90), w.r.t. the design variables are seen in equation (B.103) to (B.108), however the partial derivatives of  $I_y$ ,  $I_z$ ,  $Y$ , and  $Z$  w.r.t. the design variables are given in equation (B.53) to (B.56) and equation (B.58) to (B.61).



$$\frac{\partial Q_y}{\partial d} = t \sin(\beta) (d - t) \quad (\text{B.103})$$

$$\frac{\partial Q_z}{\partial d} = -t \sin\left(\beta - \frac{\pi}{2}\right) (d - t) \quad (\text{B.104})$$

$$\frac{\partial J_x}{\partial d} = \pi \frac{d^3 - (d - 2t)^3}{8} \quad (\text{B.105})$$

$$\frac{\partial Q_y}{\partial t} = \frac{1}{2} \sin(\beta) (d^2 - 4dt + 3t^2) \quad (\text{B.106})$$

$$\frac{\partial Q_z}{\partial t} = \frac{1}{2} (3t - d) (d - t) \sin\left(\beta - \frac{\pi}{2}\right) \quad (\text{B.107})$$

$$\frac{\partial J_x}{\partial t} = \pi \frac{(d - 2t)^3}{4} \quad (\text{B.108})$$

Since the effective width of the cross-section,  $b_1$  and  $b_2$  are piece-wise functions, the partial derivatives w.r.t. the design variables are also piece-wise functions, as shown in equation (B.109) to (B.112).

$$\frac{\partial b_1}{\partial d} = \begin{cases} \frac{1}{4} \frac{\cos(\beta)^2 (d-t) - d + 2t}{\sqrt{(\frac{1}{2}d-t)^2 - \cos(\beta)^2 (\frac{1}{2}d-\frac{1}{2}t)^2}} + \frac{1}{4} \frac{(-d+t)\cos(\beta)^2 + d}{\sqrt{\frac{1}{4}d^2 - \cos(\beta)^2 (\frac{1}{2}d-\frac{1}{2}t)^2}} & , R_m \cos(\beta) \leq r \\ \frac{1}{4} \frac{d - \cos(\beta)^2 (d-t)}{\sqrt{\frac{1}{4}d^2 - \cos(\beta)^2 (\frac{1}{2}d-\frac{1}{2}t)^2}} & , r < R_m \cos(\beta) \leq R \end{cases} \quad (\text{B.109})$$

$$\frac{\partial b_2}{\partial d} = \begin{cases} \frac{1}{4} \frac{\cos(90^\circ - \beta)^2 (d-t) - d + 2t}{\sqrt{(\frac{1}{2}d-t)^2 - \cos(90^\circ - \beta)^2 (\frac{1}{2}d-\frac{1}{2}t)^2}} + \frac{1}{4} \frac{(-d+t)\cos(90^\circ - \beta)^2 + d}{\sqrt{\frac{1}{4}d^2 - \cos(90^\circ - \beta)^2 (\frac{1}{2}d-\frac{1}{2}t)^2}} & , R_m \cos(90^\circ - \beta) \leq r \\ \frac{1}{4} \frac{d - \cos(90^\circ - \beta)^2 (d-t)}{\sqrt{\frac{1}{4}d^2 - \cos(90^\circ - \beta)^2 (\frac{1}{2}d-\frac{1}{2}t)^2}} & , r < R_m \cos(90^\circ - \beta) \leq R \end{cases} \quad (\text{B.110})$$

$$\frac{\partial b_1}{\partial t} = \begin{cases} \frac{1}{4} \frac{\cos(\beta)^2 (d-t) - 2d + 4t}{\sqrt{(\frac{1}{2}d-t)^2 - \cos(\beta)^2 (\frac{1}{2}d-\frac{1}{2}t)^2}} + \frac{1}{4} \frac{\cos(\beta)^2 (d-t)}{\sqrt{\frac{1}{4}d^2 - \cos(\beta)^2 (\frac{1}{2}d-\frac{1}{2}t)^2}} & , R_m \cos(\beta) \leq r \\ \frac{1}{4} \frac{\cos(\beta)^2 (d-t)}{\sqrt{\frac{1}{4}d^2 - \cos(\beta)^2 (\frac{1}{2}d-\frac{1}{2}t)^2}} & , r < R_m \cos(\beta) \leq R \end{cases} \quad (\text{B.111})$$

$$\frac{\partial b_2}{\partial t} = \begin{cases} \frac{1}{4} \frac{\cos(90^\circ - \beta)^2 (d-t) - 2d + 4t}{\sqrt{(\frac{1}{2}d-t)^2 - \cos(90^\circ - \beta)^2 (\frac{1}{2}d-\frac{1}{2}t)^2}} + \frac{1}{4} \frac{\cos(90^\circ - \beta)^2 (d-t)}{\sqrt{\frac{1}{4}d^2 - \cos(90^\circ - \beta)^2 (\frac{1}{2}d-\frac{1}{2}t)^2}} & , R_m \cos(90^\circ - \beta) \leq r \\ \frac{1}{4} \frac{\cos(90^\circ - \beta)^2 (d-t)}{\sqrt{\frac{1}{4}d^2 - \cos(90^\circ - \beta)^2 (\frac{1}{2}d-\frac{1}{2}t)^2}} & , r < R_m \cos(90^\circ - \beta) \leq R \end{cases} \quad (\text{B.112})$$

The partial derivatives of  $V_y$ ,  $V_z$ , and  $T_x$  are determined using the chain rule:

$$\frac{\partial V_y}{\partial x_i} = \frac{dV_y}{dI_z} \frac{\partial I_z}{\partial x_i} \quad (\text{B.113})$$

$$\frac{\partial V_z}{\partial x_i} = \frac{dV_z}{dI_y} \frac{\partial I_y}{\partial x_i} \quad (\text{B.114})$$

$$\frac{\partial T_x}{\partial x_i} = \frac{dT_x}{dJ_x} \frac{\partial J_x}{\partial x_i} \quad (\text{B.115})$$

where the total derivatives are determined as follows:

$$\frac{dV_y}{dI_z} = -E \frac{d^3v}{dx^3} \quad (\text{B.116})$$

$$\frac{dT_x}{dJ_x} = \frac{G \Delta\theta_x}{L_e} \quad (\text{B.117})$$

$$\frac{dV_z}{dI_y} = E \frac{d^3w}{dx^3} \quad (\text{B.118})$$

The expressions for the partial derivatives of  $V_y$ ,  $V_z$ , and  $T_x$  can be determined by inserting equation (B.54), (B.56), (B.59), (B.61), (B.105), (B.108), and (B.116) to (B.118) into equation (B.113) to (B.115).

By combining the above expressions according to equation (B.90), an expression for the partial derivative of the shear stress w.r.t. design variables can be obtained. However, since some of the derivatives are piece-wise functions, the partial derivative of the shear stress will also be a piece-wise function.

### Sensitivity w.r.t. displacements

The partial derivative of the shear stress w.r.t. displacements is shown in equation (B.119), where the chain rule have been applied.

$$\frac{\partial \tau_A}{\partial \{D_e\}} = \frac{d\tau_A}{dV_y} \frac{\partial V_y}{\partial \{D_e\}} + \frac{d\tau_A}{dV_z} \frac{\partial V_z}{\partial \{D_e\}} + \frac{d\tau_A}{dT_x} \frac{\partial T_x}{\partial \{D_e\}} \quad (\text{B.119})$$

The total derivatives of  $\tau_A$  w.r.t.  $V_y$ ,  $V_z$ , and  $T_x$  are expressed in equation (B.91), (B.97), and (B.95). The partial derivatives of  $V_y$ ,  $V_z$ , and  $T_x$  w.r.t. displacements are shown in equation (B.120) to (B.122).

$$\frac{\partial V_y}{\partial \{D_e\}} = \frac{dV_y}{d \frac{d^3v}{dx^3}} \frac{\partial \frac{d^3v}{dx^3}}{\partial \{D_e\}} \quad (\text{B.120})$$

$$\frac{\partial V_z}{\partial \{D_e\}} = \frac{dV_z}{d \frac{d^3w}{dx^3}} \frac{\partial \frac{d^3w}{dx^3}}{\partial \{D_e\}} \quad (\text{B.121})$$

$$\frac{\partial T_x}{\partial \{D_e\}} = \frac{dT_x}{d\Delta\theta_x} \frac{\partial \Delta\theta_x}{\partial \{D_e\}} \quad (\text{B.122})$$

where the total derivatives in equation (B.120) to (B.122) are expressed below:

$$\frac{dV_y}{d \frac{d^3v}{dx^3}} = -E I_z \quad (\text{B.123})$$

$$\frac{dV_z}{d \frac{d^3w}{dx^3}} = E I_y \quad (\text{B.124})$$

$$\frac{dT_x}{d\Delta\theta_x} = \frac{G J_x}{L_e} \quad (\text{B.125})$$

The partial derivatives, in equation (B.120) to (B.122), w.r.t. displacements are shown in

equation (B.126) to (B.128).

$$\frac{\partial \frac{d^3 v}{dx^3}}{\partial \{D_e\}} = \left\{ \begin{array}{cccccccccccc} 0 & \frac{12}{L_e^2} & 0 & 0 & 0 & \frac{6}{L_e} & 0 & \frac{-12}{L_e^2} & 0 & 0 & 0 & \frac{6}{L_e} \end{array} \right\}^T \quad (\text{B.126})$$

$$\frac{\partial \frac{d^3 w}{dx^3}}{\partial \{D_e\}} = \left\{ \begin{array}{cccccccccccc} 0 & 0 & \frac{-12}{L_e^2} & 0 & \frac{6}{L_e} & 0 & 0 & 0 & \frac{12}{L_e^2} & 0 & \frac{6}{L_e} & 0 \end{array} \right\}^T \quad (\text{B.127})$$

$$\frac{\partial \Delta \theta_x}{\partial \{D_e\}} = \left\{ \begin{array}{cccccccccccc} 0 & 0 & 0 & -1 & 0 & 0 & 0 & 0 & 0 & 0 & 1 & 0 \end{array} \right\}^T \quad (\text{B.128})$$

By inserting the above expressions into equation (B.119), the partial derivative of the shear stress w.r.t. displacements are given in equation (B.129).

$$\frac{\partial \tau_A}{\partial \{D_e\}} = \left\{ \begin{array}{c} 0 \\ -\frac{3 E t \sin(\beta) (d-t)^2}{L_e^2 b_1} \\ -\frac{3 E t \cos(\beta) (d-t)^2}{L_e^2 b_2} \\ -\frac{G (\cos(\beta) - \sin(\beta)) (d-t)}{2 L_e} \\ \frac{3 E t \cos(\beta) (d-t)^2}{L_e^2 b_2} \\ -\frac{3 E t \sin(\beta) (d-t)^2}{L_e^2 b_1} \\ 0 \\ \frac{3 E t \sin(\beta) (d-t)^2}{L_e^2 b_1} \\ \frac{3 E t \cos(\beta) (d-t)^2}{L_e^2 b_2} \\ \frac{G (\cos(\beta) - \sin(\beta)) (d-t)}{2 L_e} \\ \frac{3 E t \cos(\beta) (d-t)^2}{L_e^2 b_2} \\ -\frac{3 E t \sin(\beta) (d-t)^2}{L_e^2 b_1} \end{array} \right\} \quad (\text{B.129})$$



# Plot for verification of design sensitivity analysis



In this appendix, the sensitivities w.r.t design variables  $t_1$ ,  $d_2$ , and  $t_2$  are presented. These sensitivities are determined using the central difference method and the direct differentiation method. The central difference method have been applied for the plots on the left side of the page, whereas the plots to the right are determined using the direct differentiation method. This appendix show supplementary plots to the verification in chapter 7.

## C.1 Sensitivity of displacements

In figure C.1, C.3, and C.5 are the displacement sensitivities shown, using the central difference method. The displacement sensitivities using the direct differentiation method are shown in figure C.2, C.4, and C.6.

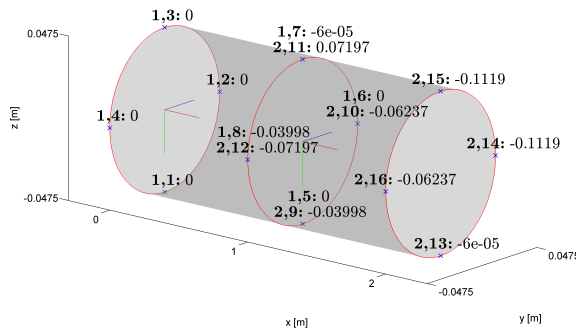


**Figure C.1** Sensitivity of displacements w.r.t. outer diameter,  $t_1$ , determined using the central difference method, in meters.

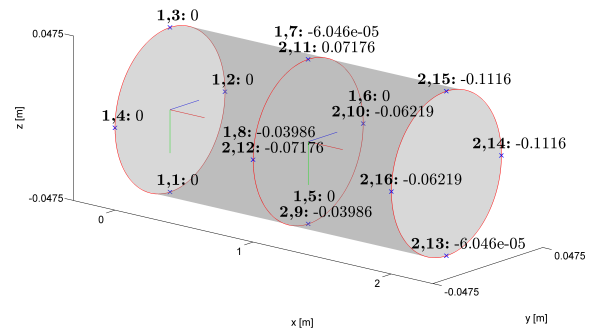


**Figure C.2** Sensitivity of displacements w.r.t. outer diameter,  $t_1$ , determined using the direct differentiation method, in meters.

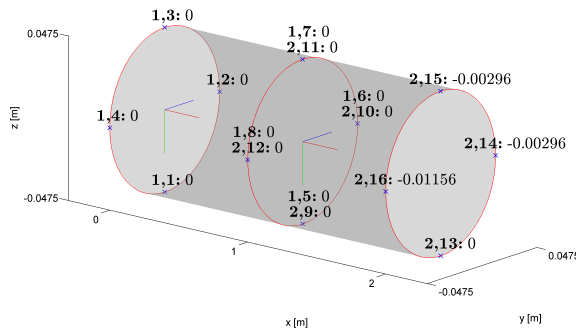


**Figure C.3** Sensitivity of displacements w.r.t. outer diameter,  $d_2$ , determined using the central difference method, in meters.

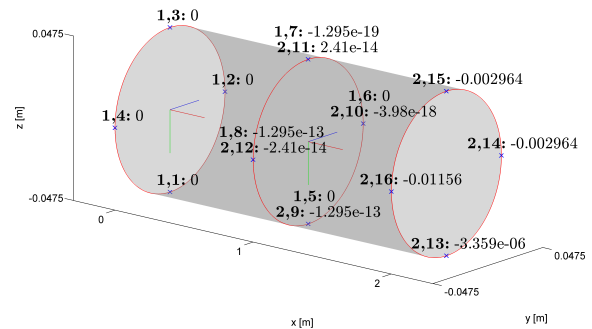


**Figure C.4** Sensitivity of displacements w.r.t. outer diameter,  $d_2$ , determined using the direct differentiation method, in meters.

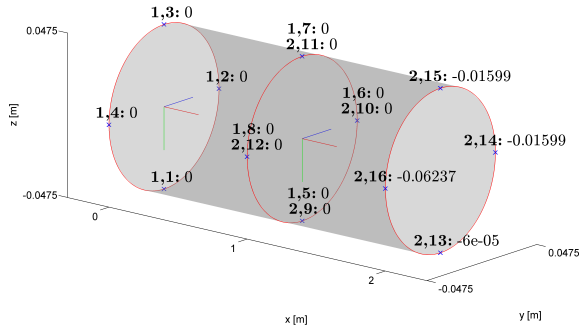


**Figure C.5** Sensitivity of displacements w.r.t. outer diameter,  $t_2$ , determined using the central difference method, in meters.

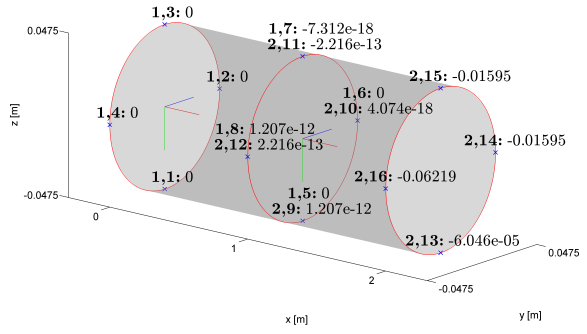


**Figure C.6** Sensitivity of displacements w.r.t. outer diameter,  $t_2$ , determined using the direct differentiation method, in meters.

## C.2 Sensitivity of normal stress

In figure C.7, C.9, and C.11 are the normal stress sensitivities shown, using the central difference method. The normal stress sensitivities using the direct differentiation method are shown in figure C.8, C.10, and C.12.

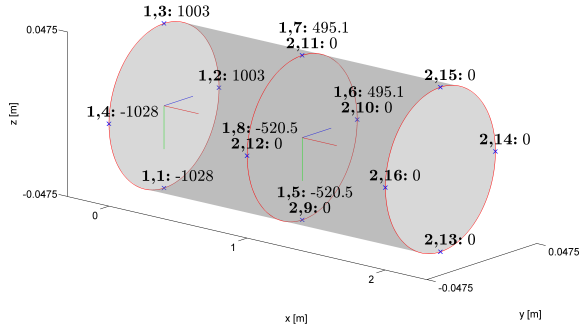


**Figure C.7** Sensitivity of normal stress w.r.t. outer diameter,  $t_1$ , determined using the central difference method, in MPa/m.

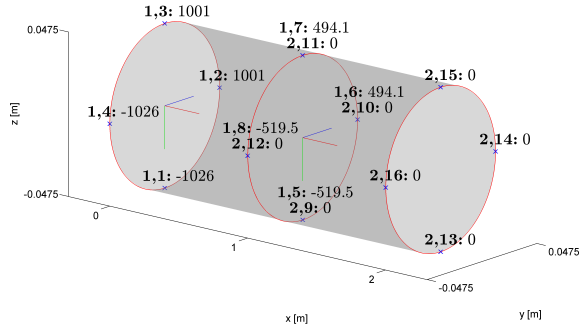


**Figure C.8** Sensitivity of normal stress w.r.t. outer diameter,  $t_1$ , determined using the direct differentiation method, in MPa/m.

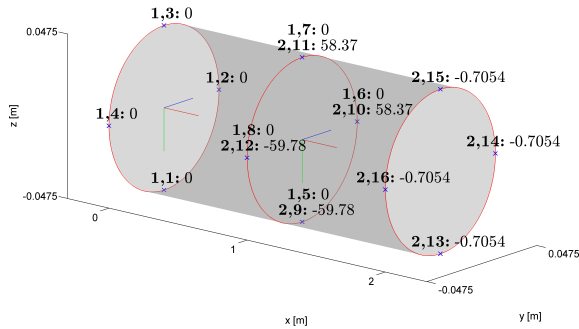


**Figure C.9** Sensitivity of normal stress w.r.t. outer diameter,  $d_2$ , determined using the central difference method, in MPa/m.

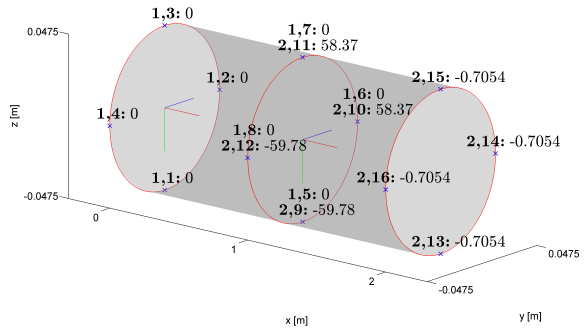


**Figure C.10** Sensitivity of normal stress w.r.t. outer diameter,  $d_2$ , determined using the direct differentiation method, in MPa/m.

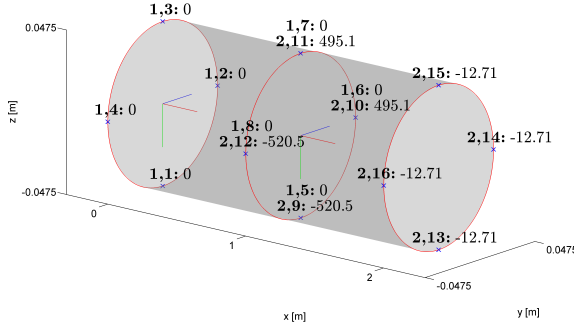


**Figure C.11** Sensitivity of normal stress w.r.t. outer diameter,  $t_2$ , determined using the central difference method, in MPa/m.

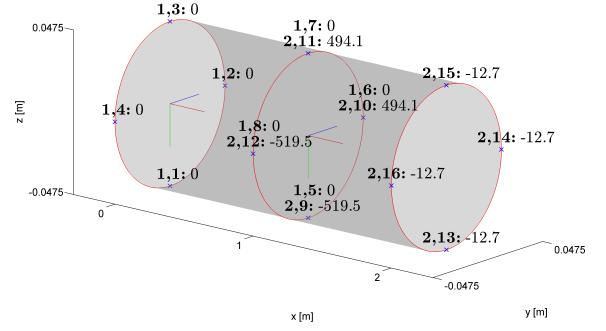


**Figure C.12** Sensitivity of normal stress w.r.t. outer diameter,  $t_2$ , determined using the direct differentiation method, in MPa/m.

### C.3 Sensitivity of shear stress

In figure C.13, C.15, and C.17 are the shear stress sensitivities shown, using the central difference method. The shear stress sensitivities using the direct differentiation method are shown in figure C.14, C.16, and C.18.

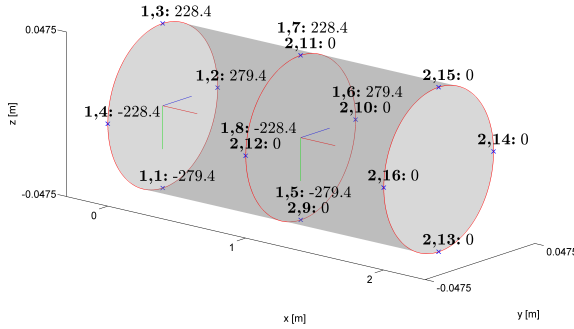


**Figure C.13** Sensitivity of shear stress w.r.t. outer diameter,  $t_1$ , determined using the central difference method, in MPa/m.

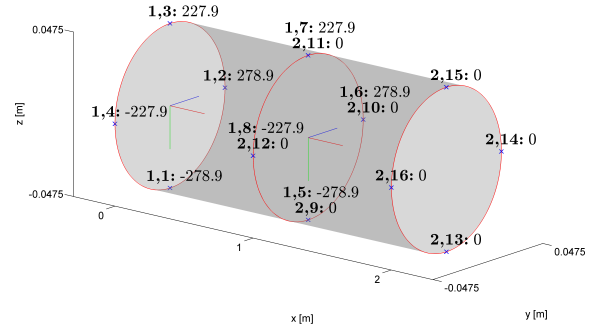


**Figure C.14** Sensitivity of shear stress w.r.t. outer diameter,  $t_1$ , determined using the direct differentiation method, in MPa/m.

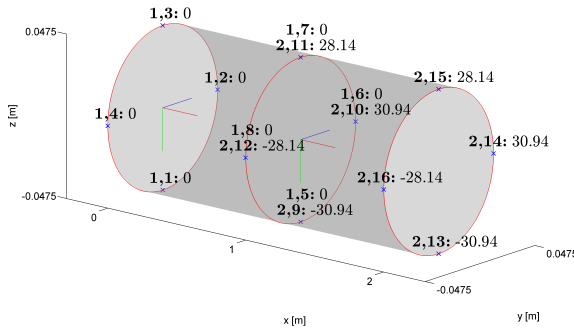


**Figure C.15** Sensitivity of shear stress w.r.t. outer diameter,  $d_2$ , determined using the central difference method, in MPa/m.

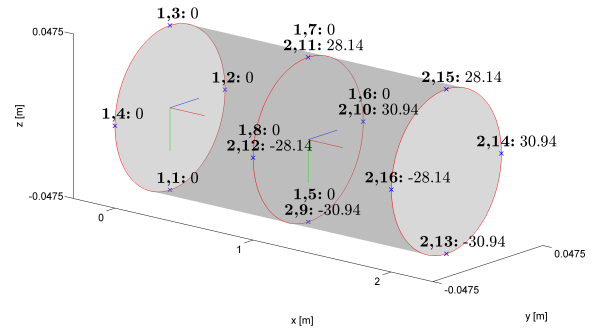


**Figure C.16** Sensitivity of shear stress w.r.t. outer diameter,  $d_2$ , determined using the direct differentiation method, in MPa/m.

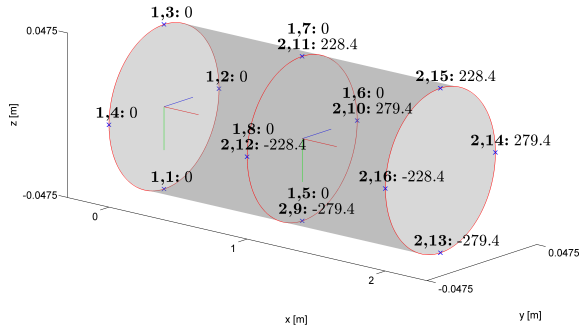


**Figure C.17** Sensitivity of shear stress w.r.t. outer diameter,  $t_2$ , determined using the central difference method, in MPa/m.

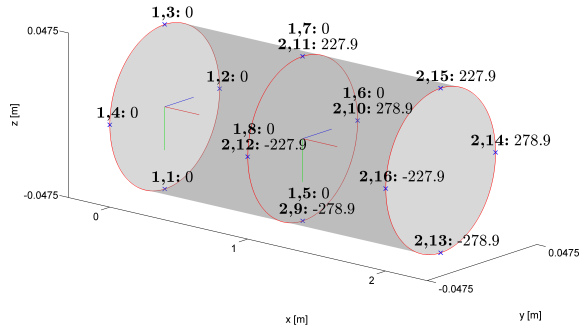


**Figure C.18** Sensitivity of shear stress w.r.t. outer diameter,  $t_2$ , determined using the direct differentiation method, in MPa/m.

## C.4 Sensitivity of constraint function

In figure C.19, C.21, and C.23 are the damage sensitivities shown, using the central difference method. The damage sensitivities using the direct differentiation method are shown in figure C.20, C.22, and C.24.

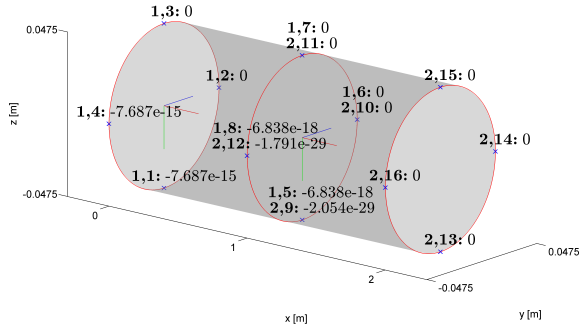


**Figure C.19** Sensitivity of constraint w.r.t. outer diameter,  $t_1$ , determined using the central difference method.

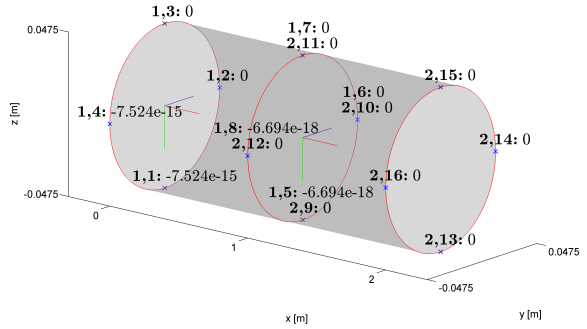


**Figure C.20** Sensitivity of constraint w.r.t. outer diameter,  $t_1$ , determined using the direct differentiation method.

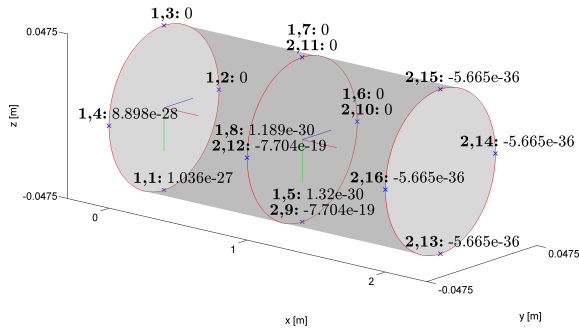


**Figure C.21** Sensitivity of constraint w.r.t. outer diameter,  $d_2$ , determined using the central difference method.

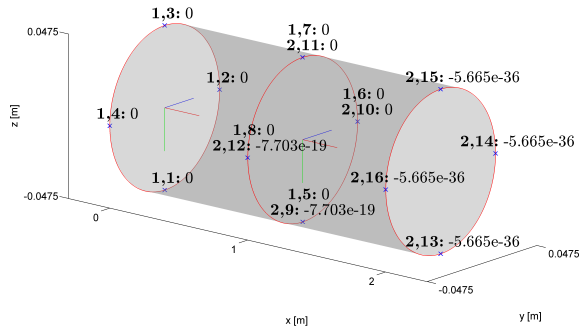


**Figure C.22** Sensitivity of constraint w.r.t. outer diameter,  $d_2$ , determined using the direct differentiation method.



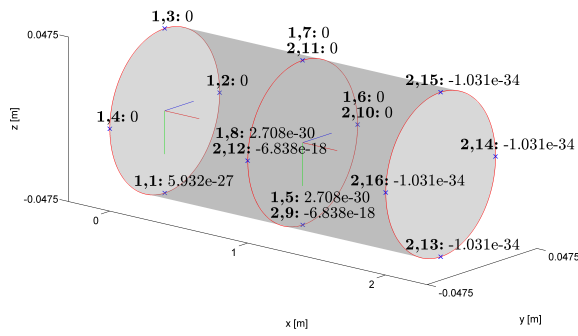


**Figure C.23** Sensitivity of constraint w.r.t. outer diameter,  $t_2$ , determined using the central difference method.

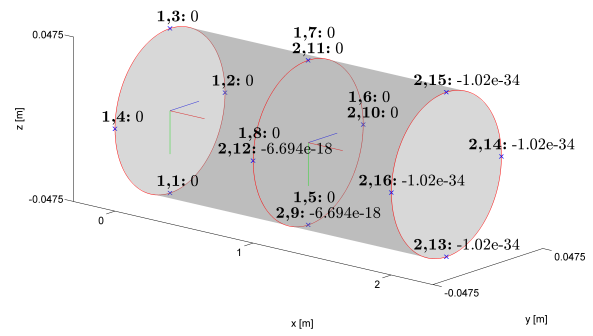


**Figure C.24** Sensitivity of constraint w.r.t. outer diameter,  $t_2$ , determined using the direct differentiation method.



In this appendix, the files which are to be found on the appended CD, are listed.

- **ANSYS**<sup>1</sup>
  - **PedalInput**  
Folder which contains geometry file generated from MATLAB.
  - **JacketStructureModel.inp**  
Static analysis of the selected geometry, which is generated by 'OutPutMatlab-GeoToANSYS.m'.
- **MATLAB**
  - **Functions**  
Folder which contains various functions.
  - **Geometry**  
Folder which contains geometry file.
  - **JacketStructureMain.m**  
Script which calculates the displacements, stresses and natural frequencies of the jacket structure model.
  - **LoadHistoryReduction.m**  
Script which reduces the load history, by removing non-turning point values.
  - **MWBrainflowTest.m**  
Script which counts the reversals, that is shown graphically in section 4.2.
  - **OutPutMatlabGeoToANSYS.m**  
Function which translates the geometry used in the MATLAB code into an ANSYS APDL input script. This function has the geometry file name as input.
  - **SensitivityTest.m**  
Script which compares the design sensitivities determined using the direct differentiation method and the central difference method.
  - **SimpleSLPoptimisation.m**  
Script which executes the SLP optimisation algorithm, where the mass of the cantilever beam model is minimised.
- **Report.pdf**

---

<sup>1</sup>It is recommended to copy the script to a folder on the hard drive of the computer. To run the script, the current working directory has to be changed to match the folder of which this script is run from. This is done using this command: /CWD,'path to working directory'.